

Single Intermediate Vector Boson production in e^+e^- collisions at $\sqrt{s} = 183 - 209$ GeV

DELPHI Collaboration

Abstract

The production of single charged and neutral intermediate vector bosons in e^+e^- collisions has been studied in the data collected by the DELPHI experiment at LEP at centre-of-mass energies between 183 and 209 GeV, corresponding to an integrated luminosity of about 640 pb^{-1} . The measured cross-sections for the reactions, determined in limited kinematic regions, are in agreement with the Standard Model predictions.

(Eur. Phys. J. C45 (2006) 273-289)

J.Abdallah²⁵, P.Abreu²², W.Adam⁵¹, P.Adzic¹¹, T.Albrecht¹⁷, T.Alderweireld², R.Aleman-Fernandez⁸, T.Allmendinger¹⁷, P.P.Allport²³, U.Amaldi²⁹, N.Amapane⁴⁵, S.Amato⁴⁸, E.Anashkin³⁶, A.Andreazza²⁸, S.Andringa²², N.Anjos²², P.Antilogus²⁵, W-D.Apel¹⁷, Y.Arnoud¹⁴, S.Ask²⁶, B.Asman⁴⁴, J.E.Augustin²⁵, A.Augustinus⁸, P.Baillon⁸, A.Ballestrero⁴⁶, P.Bambade²⁰, R.Barbier²⁷, D.Bardin¹⁶, G.J.Barker¹⁷, A.Baroncelli³⁹, M.Battaglia⁸, M.Baumbach²⁵, K-H.Becks⁵³, M.Begalli⁶, A.Behrmann⁵³, E.Ben-Haim²⁰, N.Benekos³², A.Benvenuti⁵, C.Berat¹⁴, M.Berggren²⁵, L.Berntzon⁴⁴, D.Bertrand², M.Besancon⁴⁰, N.Besson⁴⁰, D.Bloch⁹, M.Blom³¹, M.Bluj⁵², M.Bonesini²⁹, M.Boonekamp⁴⁰, P.S.L.Booth²³, G.Borisov²¹, O.Botner⁴⁹, B.Bouquet²⁰, T.J.V.Bowcock²³, I.Boyko¹⁶, M.Bracko⁴³, R.Brenner⁴⁹, E.Brodet³⁵, P.Bruckman¹⁸, J.M.Brunet⁷, P.Buschmann⁵³, M.Calvi²⁹, T.Camporesi⁸, V.Canale³⁸, F.Carena⁸, N.Castro²², F.Cavallo⁵, M.Chapkin⁴², Ph.Charpentier⁸, P.Checchia³⁶, R.Chierici⁸, P.Chliapnikov⁴², J.Chudoba⁸, S.U.Chung⁸, K.Cieslik¹⁸, P.Collins⁸, R.Contri¹³, G.Cosme²⁰, F.Cossutti⁴⁷, M.J.Costa⁵⁰, D.Crennell³⁷, J.Cuevas³⁴, J.D'Hondt², J.Dalmau⁴⁴, T.da Silva⁴⁸, W.Da Silva²⁵, G.Della Ricca⁴⁷, A.De Angelis⁴⁷, W.De Boer¹⁷, C.De Clercq², B.De Lotto⁴⁷, N.De Maria⁴⁵, A.De Min³⁶, L.de Paula⁴⁸, L.Di Ciccio³⁸, A.Di Simone³⁹, K.Doroba⁵², J.Drees^{53,8}, G.Eigen⁴, T.Ekelof⁴⁹, M.Ellert⁴⁹, M.Elsing⁸, M.C.Espirito Santo²², G.Fanourakis¹¹, D.Fassouliotis^{11,3}, M.Feindt¹⁷, J.Fernandez⁴¹, A.Ferre⁵⁰, F.Ferro¹³, U.Flagmeyer⁵³, H.Foeth⁸, E.Fokitis³², F.Fulda-Quenzer²⁰, J.Fuster⁵⁰, M.Gandelman⁴⁸, C.Garcia⁵⁰, Ph.Gavillet⁸, E.Gazis³², R.Gokieli^{8,52}, B.Golob⁴³, G.Gomez-Ceballos⁴¹, P.Goncalves²², E.Graziani³⁹, G.Grosdidier²⁰, K.Grzelak⁵², J.Guy³⁷, C.Haag¹⁷, A.Hallgren⁴⁹, K.Hamacher⁵³, K.Hamilton³⁵, S.Haug³³, F.Hauler¹⁷, V.Hedberg²⁶, M.Hennecke¹⁷, H.Herr⁸, J.Hoffman⁵², S-O.Holmgren⁴⁴, P.J.Holt⁸, M.A.Houlden²³, K.Hultqvist⁴⁴, J.N.Jackson²³, G.Jarlskog²⁶, P.Jarry⁴⁰, D.Jeans³⁵, E.K.Johansson⁴⁴, P.D.Johansson⁴⁴, P.Jonsson²⁷, C.Joram⁸, L.Jungermann¹⁷, F.Kapusta²⁵, S.Katsanevas²⁷, E.Katsoufis³², G.Kernel⁴³, B.P.Kersevan^{8,43}, U.Kerzel¹⁷, B.T.King²³, N.J.Kjaer⁸, P.Kluit³¹, P.Kokkinias¹¹, C.Kourkoulis³, O.Kouznetsov¹⁶, Z.Krumstein¹⁶, M.Kucharczyk¹⁸, J.Lamsa¹, G.Leder⁵¹, F.Ledroit¹⁴, L.Leinonen⁴⁴, R.Leitner³⁰, J.Lemmon², V.Lepeltier²⁰, T.Lesiak¹⁸, W.Liebig⁵³, D.Liko⁵¹, A.Lipniacka⁴⁴, J.H.Lopes⁴⁸, J.M.Lopez³⁴, D.Loukas¹¹, P.Lutz⁴⁰, L.Lyons³⁵, J.MacNaughton⁵¹, A.Malek⁵³, S.Maltesos³², F.Mandl⁵¹, J.Marco⁴¹, R.Marco⁴¹, B.Marechal⁴⁸, M.Margoni³⁶, J-C.Marin⁸, C.Mariotti⁸, A.Markou¹¹, C.Martinez-Rivero⁴¹, J.Masik¹², N.Mastroiannopoulos¹¹, F.Matorras⁴¹, C.Matteuzzi²⁹, F.Mazzucato³⁶, M.Mazzucato³⁶, R.Mc Nulty²³, C.Meroni²⁸, E.Migliore⁴⁵, W.Mitaroff⁵¹, U.Mjoernmark²⁶, T.Moa⁴⁴, M.Moch¹⁷, K.Moenig^{8,10}, R.Monge¹³, J.Montenegro³¹, D.Moraes⁴⁸, S.Moreno²², P.Morettini¹³, U.Mueller⁵³, K.Muenich⁵³, M.Mulders³¹, L.Mundim⁶, W.Murray³⁷, B.Muryn¹⁹, G.Myatt³⁵, T.Myklebust³³, M.Nassiakou¹¹, F.Navarria⁵, K.Nawrocki⁵², R.Nicolaidou⁴⁰, M.Nikolenko^{16,9}, A.Oblakowska-Mucha¹⁹, V.Obratzov⁴², A.Olshevski¹⁶, A.Onofre²², R.Orava¹⁵, K.Osterberg¹⁵, A.Ouraou⁴⁰, A.Oyanguren⁵⁰, M.Paganoni²⁹, S.Paiano⁵, J.P.Palacios²³, H.Palka¹⁸, Th.D.Papadopoulou³², L.Pape⁸, C.Parkes²⁴, F.Parodi¹³, U.Parzefall⁸, A.Passeri³⁹, O.Passon⁵³, L.Peralta²², V.Perepelitsa⁵⁰, A.Perrotta⁵, A.Petrolini¹³, J.Piedra⁴¹, L.Pieri³⁹, F.Pierre⁴⁰, M.Pimenta²², E.Piotto⁸, T.Podobnik⁴³, V.Poireau⁸, M.E.Pol⁶, G.Polok¹⁸, V.Pozdniakov¹⁶, N.Pukhaeva^{2,16}, A.Pullia²⁹, J.Rames¹², A.Read³³, P.Rebecchi⁸, J.Rehn¹⁷, D.Reid³¹, R.Reinhardt⁵³, P.Renton³⁵, F.Richard²⁰, J.Ridky¹², M.Rivero⁴¹, D.Rodriguez⁴¹, A.Romero⁴⁵, P.Ronchese³⁶, P.Roudeau²⁰, T.Rovelli⁵, V.Ruhlmann-Kleider⁴⁰, D.Ryabtchikov⁴², A.Sadovsky¹⁶, L.Salmi¹⁵, J.Salt⁵⁰, C.Sander¹⁷, A.Savoy-Navarro²⁵, U.Schwickerath⁸, A.Segar³⁵, R.Sekulin³⁷, M.Siebel⁵³, A.Sisakian¹⁶, G.Smadja²⁷, O.Smirnova²⁶, A.Sokolov⁴², A.Sopczak²¹, R.Sosnowski⁵², T.Spassov⁸, M.Stanitzki¹⁷, A.Stocchi²⁰, J.Strauss⁵¹, B.Stugu⁴, M.Szczekowski⁵², M.Szeptycka⁵², T.Szumak¹⁹, T.Tabarelli²⁹, A.C.Taffard²³, F.Tegenfeldt⁴⁹, J.Timmermans³¹, L.Tkatchev¹⁶, M.Tobin²³, S.Todorovova¹², B.Tome²², A.Tonazzo²⁹, P.Tortosa⁵⁰, P.Travnicek¹², D.Treille⁸, G.Tristram⁷, M.Trochimczuk⁵², C.Troncon²⁸, M-L.Turluer⁴⁰, I.A.Tyapkin¹⁶, P.Tyapkin¹⁶, S.Tzamarias¹¹, V.Uvarov⁴², G.Valenti⁵, P.Van Dam³¹, J.Van Eldik⁸, N.van Remortel¹⁵, I.Van Vulpen⁸, G.Vegni²⁸, F.Veloso²², W.Venus³⁷, P.Verdier²⁷, V.Verzi³⁸, D.Vilanova⁴⁰, L.Vitale⁴⁷, V.Vrba¹², H.Wahlen⁵³, A.J.Washbrook²³, C.Weiser¹⁷, D.Wicke⁸, J.Wickens²,

G.Wilkinson³⁵, M.Winter⁹, M.Witek¹⁸, O.Yushchenko⁴², A.Zalewska¹⁸, P.Zalewski⁵², D.Zavrtanik⁴³, V.Zhuravlov¹⁶, N.I.Zimin¹⁶, A.Zintchenko¹⁶, M.Zupan¹¹

-
- ¹Department of Physics and Astronomy, Iowa State University, Ames IA 50011-3160, USA
²Physics Department, Universiteit Antwerpen, Universiteitsplein 1, B-2610 Antwerpen, Belgium
and IIHE, ULB-VUB, Pleinlaan 2, B-1050 Brussels, Belgium
and Faculté des Sciences, Univ. de l'Etat Mons, Av. Maistriau 19, B-7000 Mons, Belgium
³Physics Laboratory, University of Athens, Solonos Str. 104, GR-10680 Athens, Greece
⁴Department of Physics, University of Bergen, Allégaten 55, NO-5007 Bergen, Norway
⁵Dipartimento di Fisica, Università di Bologna and INFN, Via Irnerio 46, IT-40126 Bologna, Italy
⁶Centro Brasileiro de Pesquisas Físicas, rua Xavier Sigaud 150, BR-22290 Rio de Janeiro, Brazil
and Depto. de Física, Pont. Univ. Católica, C.P. 38071 BR-22453 Rio de Janeiro, Brazil
and Inst. de Física, Univ. Estadual do Rio de Janeiro, rua São Francisco Xavier 524, Rio de Janeiro, Brazil
⁷Collège de France, Lab. de Physique Corpusculaire, IN2P3-CNRS, FR-75231 Paris Cedex 05, France
⁸CERN, CH-1211 Geneva 23, Switzerland
⁹Institut de Recherches Subatomiques, IN2P3 - CNRS/ULP - BP20, FR-67037 Strasbourg Cedex, France
¹⁰Now at DESY-Zeuthen, Platanenallee 6, D-15735 Zeuthen, Germany
¹¹Institute of Nuclear Physics, N.C.S.R. Demokritos, P.O. Box 60228, GR-15310 Athens, Greece
¹²FZU, Inst. of Phys. of the C.A.S. High Energy Physics Division, Na Slovance 2, CZ-180 40, Praha 8, Czech Republic
¹³Dipartimento di Fisica, Università di Genova and INFN, Via Dodecaneso 33, IT-16146 Genova, Italy
¹⁴Institut des Sciences Nucléaires, IN2P3-CNRS, Université de Grenoble 1, FR-38026 Grenoble Cedex, France
¹⁵Helsinki Institute of Physics and Department of Physical Sciences, P.O. Box 64, FIN-00014 University of Helsinki, Finland
¹⁶Joint Institute for Nuclear Research, Dubna, Head Post Office, P.O. Box 79, RU-101 000 Moscow, Russian Federation
¹⁷Institut für Experimentelle Kernphysik, Universität Karlsruhe, Postfach 6980, DE-76128 Karlsruhe, Germany
¹⁸Institute of Nuclear Physics PAN, Ul. Radzikowskiego 152, PL-31142 Krakow, Poland
¹⁹Faculty of Physics and Nuclear Techniques, University of Mining and Metallurgy, PL-30055 Krakow, Poland
²⁰Université de Paris-Sud, Lab. de l'Accélérateur Linéaire, IN2P3-CNRS, Bât. 200, FR-91405 Orsay Cedex, France
²¹School of Physics and Chemistry, University of Lancaster, Lancaster LA1 4YB, UK
²²LIP, IST, FCUL - Av. Elias Garcia, 14-1º, PT-1000 Lisboa Codex, Portugal
²³Department of Physics, University of Liverpool, P.O. Box 147, Liverpool L69 3BX, UK
²⁴Dept. of Physics and Astronomy, Kelvin Building, University of Glasgow, Glasgow G12 8QQ
²⁵LPNHE, IN2P3-CNRS, Univ. Paris VI et VII, Tour 33 (RdC), 4 place Jussieu, FR-75252 Paris Cedex 05, France
²⁶Department of Physics, University of Lund, Sölvegatan 14, SE-223 63 Lund, Sweden
²⁷Université Claude Bernard de Lyon, IPNL, IN2P3-CNRS, FR-69622 Villeurbanne Cedex, France
²⁸Dipartimento di Fisica, Università di Milano and INFN-MILANO, Via Celoria 16, IT-20133 Milan, Italy
²⁹Dipartimento di Fisica, Univ. di Milano-Bicocca and INFN-MILANO, Piazza della Scienza 2, IT-20126 Milan, Italy
³⁰IPNP of MFF, Charles Univ., Areal MFF, V Holesovickach 2, CZ-180 00, Praha 8, Czech Republic
³¹NIKHEF, Postbus 41882, NL-1009 DB Amsterdam, The Netherlands
³²National Technical University, Physics Department, Zografou Campus, GR-15773 Athens, Greece
³³Physics Department, University of Oslo, Blindern, NO-0316 Oslo, Norway
³⁴Dpto. Física, Univ. Oviedo, Avda. Calvo Sotelo s/n, ES-33007 Oviedo, Spain
³⁵Department of Physics, University of Oxford, Keble Road, Oxford OX1 3RH, UK
³⁶Dipartimento di Fisica, Università di Padova and INFN, Via Marzolo 8, IT-35131 Padua, Italy
³⁷Rutherford Appleton Laboratory, Chilton, Didcot OX11 0QX, UK
³⁸Dipartimento di Fisica, Università di Roma II and INFN, Tor Vergata, IT-00173 Rome, Italy
³⁹Dipartimento di Fisica, Università di Roma III and INFN, Via della Vasca Navale 84, IT-00146 Rome, Italy
⁴⁰DAPNIA/Service de Physique des Particules, CEA-Saclay, FR-91191 Gif-sur-Yvette Cedex, France
⁴¹Instituto de Física de Cantabria (CSIC-UC), Avda. los Castros s/n, ES-39006 Santander, Spain
⁴²Inst. for High Energy Physics, Serpukov P.O. Box 35, Protvino, (Moscow Region), Russian Federation
⁴³J. Stefan Institute, Jamova 39, SI-1000 Ljubljana, Slovenia and Laboratory for Astroparticle Physics, Nova Gorica Polytechnic, Kostanjevska 16a, SI-5000 Nova Gorica, Slovenia, and Department of Physics, University of Ljubljana, SI-1000 Ljubljana, Slovenia
⁴⁴Fysikum, Stockholm University, Box 6730, SE-113 85 Stockholm, Sweden
⁴⁵Dipartimento di Fisica Sperimentale, Università di Torino and INFN, Via P. Giuria 1, IT-10125 Turin, Italy
⁴⁶INFN, Sezione di Torino and Dipartimento di Fisica Teorica, Università di Torino, Via Giuria 1, IT-10125 Turin, Italy
⁴⁷Dipartimento di Fisica, Università di Trieste and INFN, Via A. Valerio 2, IT-34127 Trieste, Italy and Istituto di Fisica, Università di Udine, IT-33100 Udine, Italy
⁴⁸Univ. Federal do Rio de Janeiro, C.P. 68528 Cidade Univ., Ilha do Fundão BR-21945-970 Rio de Janeiro, Brazil
⁴⁹Department of Radiation Sciences, University of Uppsala, P.O. Box 535, SE-751 21 Uppsala, Sweden
⁵⁰IFIC, Valencia-CSIC, and D.F.A.M.N., U. de Valencia, Avda. Dr. Moliner 50, ES-46100 Burjassot (Valencia), Spain
⁵¹Institut für Hochenergiephysik, Österr. Akad. d. Wissensch., Nikolsdorfergasse 18, AT-1050 Vienna, Austria
⁵²Inst. Nuclear Studies and University of Warsaw, Ul. Hoza 69, PL-00681 Warsaw, Poland
⁵³Fachbereich Physik, University of Wuppertal, Postfach 100 127, DE-42097 Wuppertal, Germany

1 Introduction

The production of four-fermion final states becomes increasingly important in e^+e^- collisions at centre-of-mass energies above the Z pole. The full set of Feynman diagrams must be considered, but particular topologies receive their dominant contribution from a subset of them (cf. Figure 1, taken from reference [1], for the standard definition of the different graphs). As the centre-of-mass energy increases, the dominant processes leading to production of vector bosons are represented by the bremsstrahlung and fusion diagrams with the production of a single vector boson¹ ($e^+e^- \rightarrow e^-\bar{\nu}_e W^+$, $e^+e^- \rightarrow e^+e^-\gamma^*/Z$), and the conversion and non-Abelian annihilation diagrams leading to doubly resonant production ($e^+e^- \rightarrow W^+W^-$, $e^+e^- \rightarrow ZZ$). Single resonant production is dominated by the bremsstrahlung process, which proceeds through the scattering of a quasi-real photon ($q_\gamma^2 \sim 0$) radiated from an incoming e^- on an e^+ of the other beam, i.e.: $\gamma e^+ \rightarrow \bar{\nu}_e W^+$, $\gamma e^+ \rightarrow e^+ Z$ [2]. The resulting topology is characterized by the e^- which radiates the quasi-real photon being predominantly lost along the beam line.

The integrated luminosity delivered by the LEP collider in the runs at centre-of-mass energies $\sqrt{s} = 183 - 209$ GeV (LEP2) allowed, for the first time, measurements of the cross-section of single boson production and not just the observation of individual events. The evaluation of the Standard Model cross-sections for this process requires the computation of the full set of Feynman diagrams and, to deal with the collinear singularity corresponding to the electron lost along the beam line, the use of fully massive matrix elements. Moreover the different scales of the couplings in the process and the scale for the QED initial state radiation (ISR) should be properly accounted for to provide a reliable prediction. Therefore this process was taken as a benchmark when comparing the different calculations used to describe four-fermion physics at LEP2 [3]. In addition, because of the large missing energy in the final state, single boson production is a background when probing for new physics as in the search for the Higgs boson in the $H\nu\bar{\nu}$ channel or for physics beyond the Standard Model [4]. Therefore the measurement of its cross-section is an important check that the background in these searches is correctly modelled. By itself, single- W production provides access to the measurement of the trilinear gauge couplings at the $WW\gamma$ vertex: this measurement, in combination with other physics channels, has been made by the DELPHI Collaboration and is reported elsewhere [5]. Finally, single boson production is interesting as it will be the dominant source of weak boson production at a forthcoming Linear Collider.

Single boson production is investigated in this paper in five different final states: $e^-\bar{\nu}_e q\bar{q}'$, $e^-\bar{\nu}_e \mu^+\nu_\mu$ and $e^-\bar{\nu}_e e^+\nu_e$ for single- W production, $e^-e^+q\bar{q}$ and $e^-e^+\mu^-\mu^+$ for single- Z production. Cross-sections are measured using the data collected by the DELPHI experiment at centre-of-mass energies ranging from 183 to 209 GeV with a corresponding integrated luminosity of about 640 pb^{-1} . Compared to the results reported by the DELPHI Collaboration in [6], those reported here are based on a larger sample, a better data processing and an improved description of the simulated events (see below). Therefore they update and supersede those already reported in [6]. Results on single boson processes have been published by the other LEP experiments in [7,8] for single- W and in [7–9] for single- Z production.

The criteria for the selection of the events are mainly based on the information from the tracking system, the calorimeters and the muon chambers of the DELPHI detector. A detailed description of the DELPHI apparatus and its performance can be found in [10]. The detector has remained essentially unchanged in the LEP2 phase, except for upgrades

¹Charge conjugate states are implied throughout the text.

of the Vertex Detector [11] and the addition of a set of scintillation counters to veto photons in the blind regions of the electromagnetic calorimetry at polar angles² $\theta \simeq 40^\circ$, $\theta \simeq 90^\circ$ and $\theta \simeq 140^\circ$. The main tracking device was the Time Projection Chamber (TPC). One of the sectors (1/12 of the azimuthal acceptance) of the TPC, hereafter indicated as S6, was not fully operational during the last period of data taking at $\sqrt{s} = 207$ GeV (about 50 pb^{-1}). The data with the TPC sector down were analysed separately, with the performance of the analysis being evaluated on dedicated simulation samples, where this effect was explicitly taken into account.

This paper is organized as follows. Section 2 introduces the definition of the single boson processes in terms of the four-fermion final states. In Sections 3 and 4 the selection of the events and the extraction of the single- W and single- Z cross-sections are presented. In Section 5 the comparison of measured cross-sections with the predictions of the Standard Model is performed for all the single boson final states.

2 Definition of the signal and simulation

Single boson production is investigated in this paper through four-fermion final states, $e^- \bar{\nu}_e f \bar{f}'$ and $e^+ e^- f \bar{f}'$. These final states receive contributions not only from single resonant diagrams but also from doubly resonant production, conversion diagrams and multiperipheral processes (Figure 1, according to the convention of [1]). To enhance the single boson production contribution, and to enable consistent comparisons and combinations between the experiments at LEP, the cross-sections have been defined in the limited kinematic regions described below.

$e\nu_e W$ channel: The four-fermion final states $e^- \bar{\nu}_e q \bar{q}'$ and $e^- \bar{\nu}_e l^+ \nu_l$ ($l = \mu, \tau$) can be produced both via single- W production, referred to as $e\nu_e W$ in the following, or via W -pair production. A distinctive feature of $e\nu_e W$ is the fact that the distribution of the electron direction is strongly peaked at small polar angles (θ_e) with respect to the incoming electron beam direction. Based on this consideration, the $e\nu_e W$ signal was defined by the complete t -channel subset³ of the Feynman diagrams contributing to the $e^- \bar{\nu}_e q \bar{q}'$ and $e^- \bar{\nu}_e l^+ \nu_l$ final states with additional kinematic selections to exclude the regions of the phase space dominated by multiperipheral diagrams, where the cross-section calculation is affected by large uncertainties. The signal region was therefore defined as follows:

$$\begin{aligned} m_{q\bar{q}'} &> 45 \text{ GeV}/c^2 & \text{for} & \quad e^- \bar{\nu}_e q \bar{q}', \\ E_{l^+} &> 20 \text{ GeV} & \text{for} & \quad e^- \bar{\nu}_e l^+ \nu_l \quad (l^+ = \mu^+, \tau^+), \end{aligned} \quad (1)$$

where $m_{q\bar{q}'}$ is the $q\bar{q}'$ invariant mass and E_{l^+} the lepton energy. Single- W production accounts for more than 80% of all $e^- \bar{\nu}_e q \bar{q}'$ and $e^- \bar{\nu}_e l^+ \nu_l$ events in the kinematic region defined above.

$e\nu_e e\nu_e$ channel: In the kinematic region with one electron lost in the forward direction, this final state receives, besides single- W production, a large contribution from single- Z production (with $Z \rightarrow \nu_e \bar{\nu}_e$) and from the interference between single- W and single- Z processes. The contribution of this channel to the $e\nu_e W$ signal was also defined

²In the reference frame used in DELPHI the z axis was oriented along the incoming e^- beam, θ indicated the polar angle and ϕ the azimuthal angle.

³The t -channel subset consists of the bremsstrahlung, fusion and multiperipheral diagrams of Figure 1.

by the complete t -channel subset of the Feynman diagrams, in this case with the following kinematic selections:

$$|\cos \theta_{e+}| < 0.95, \quad E_{e+} > 20 \text{ GeV} \quad \text{and} \quad |\cos \theta_{e-}| > 0.95. \quad (2)$$

The $e^- \bar{\nu}_e e^+ \nu_e$ channel was not used in the determination of the single- Z production cross-section.

Zee channel: The neutral bosons are produced in the process $e\gamma \rightarrow e\gamma^*/Z$, where a quasi-real photon is radiated from one of the beam electrons and scattered off the other beam. The signature of such events is an electron in the detector, typically of low energy, recoiling against the γ^*/Z system, with the other electron usually lost in the beam-pipe. The Zee cross-section, defined for the combination of the results from all the LEP experiments, refers to the entire set of 48 graphs contributing at tree level to the $e^+e^- f\bar{f}$ ($f = q, \mu$) final state with the following restrictions in the phase space to enhance the single boson contribution⁴:

$$\begin{aligned} m_{f\bar{f}} &> 60 \text{ GeV}/c^2 \quad \text{and} \\ \theta_{e+} &> 168^\circ, \quad 60^\circ < \theta_{e-} < 168^\circ \quad \text{and} \quad E_{e-} > 3 \text{ GeV} \quad \text{for a visible electron, or} \\ \theta_{e-} &< 12^\circ, \quad 12^\circ < \theta_{e+} < 120^\circ \quad \text{and} \quad E_{e+} > 3 \text{ GeV} \quad \text{for a visible positron,} \end{aligned} \quad (3)$$

the 12° (168°) being motivated by the lower angle of the acceptance for the electron identification of the LEP experiments.

At $\sqrt{s} = 200 \text{ GeV}$, within these kinematic limits, the bremsstrahlung contribution accounts for about 97% of $e^+e^- q\bar{q}$ and 67% of $e^+e^- \mu^+\mu^-$ final states. The cut on the invariant mass was set to $60 \text{ GeV}/c^2$ because it both guarantees an efficient rejection of the multiperipheral contribution and it provides a natural separation between the γ^*ee and Zee regions, as it corresponds to the minimum of the differential $m_{f\bar{f}}$ distribution. This paper presents, for the $e^+e^- q\bar{q}$ final state, besides the above defined Zee cross-section, a measurement of the cross-section with the same acceptance cuts for e^+ and e^- but in the invariant mass range $15 < m_{q\bar{q}} < 60 \text{ GeV}/c^2$ (hereafter referred to as γ^*ee).

The $e\nu_e W$ and Zee signal samples, as predicted by the Standard Model, were simulated with the WPHACT [12] event generator. For background processes, different generators were used: KK2f [13] for $q\bar{q}(\gamma)$, $e^+e^- \rightarrow \mu^+\mu^-(\gamma)$ and $\tau^+\tau^-(\gamma)$, TEEGG [14] and BHWIDE [15] for $e^+e^- \rightarrow e^+e^-\gamma$, PYTHIA 6.143 [16] and BDK [17] for two-photon collisions. Fragmentation and hadronization for the KK2f and WPHACT samples were performed using PYTHIA 6.156. A detailed description of the simulation of four-fermion events at LEP2 as done in DELPHI is given in [18]. The generated signal and background events were passed through the detailed simulation of the DELPHI detector [10] and then processed with the same reconstruction and analysis programs as the data.

3 Single- W analysis

Both the hadronic and the leptonic final states were considered in the single- W analysis. They are characterized by the presence of two hadronic jets acoplanar with the beam or by a single lepton with large transverse momentum, respectively. The final state electron is lost in the beam pipe.

⁴Diagrams involving Higgs boson exchange are neglected. Multiperipheral processes with at least one photon resolved are excluded from the signal definition even if they are within the accepted kinematic region.

3.1 Selection of hadronic events

The experimental signature of $e^- \bar{\nu}_e q \bar{q}'$ events consists of a pair of acoplanar jets. The undetected neutrino results in a large missing momentum at large angle to the beam direction.

Other physics processes which can give rise to a similar topology are $Z(\gamma)$ with $Z \rightarrow q \bar{q}$, WW events with at least one W decaying into hadrons, other four-fermion final states from neutral current processes⁵ ($l^+ l^- q \bar{q}$, $\nu \bar{\nu} q \bar{q}$, the latter being topologically identical to the signal) and events induced by two-photon collisions, hereafter called two-photon events. Some of these processes have cross-sections larger than that of the signal by several orders of magnitude. Therefore the analysis was performed in two steps: a preselection of hadronic events and a final selection based on a Feed-Forward Artificial Neural Network [20].

A sample of hadronic events was preselected by requiring at least seven charged particles to be measured in the detector. Events from Bhabha scattering were rejected by a cut on the total electromagnetic energy, $E_{EM}/\sqrt{s} < 50\%$. The contribution from two-photon collisions was reduced by requiring the total visible energy to be larger than 20% of \sqrt{s} and the total transverse energy, computed as the sum of the moduli of the momenta of each particle projected in the plane transverse to the beam axis, to be at least 15% of \sqrt{s} . In addition, it was required that the half-opening angle of the cone around the beam axis containing 15% of the visible energy had to be larger than 10° ; two-photon collision events are concentrated in the forward regions and have low values of this variable. The background from $e^+ e^- \rightarrow q \bar{q}(\gamma)$ was reduced by requiring the polar angle of the missing momentum to satisfy the condition $|\cos \theta_{miss}| < 0.98$ and the acoplanarity⁶ to be larger than 10° . $Z(\gamma)$ events, with $Z \rightarrow q \bar{q}$, were further suppressed by vetoing events with electromagnetic clusters with energy larger than 45 GeV or, if the ISR photon escaped undetected in the dead region between the barrel and end-cap electromagnetic calorimeters ($\theta \sim 40^\circ$), by vetoing events with signals in the hermeticity counters in a cone of 30° around the direction of the missing momentum. Selections on the maximum total multiplicity of charged and neutral tracks (< 50) and on the visible mass (between 30 and 100 GeV/ c^2) were applied to suppress the residual contamination of multi-jet events from WW or NC processes. Finally, WW events with one W decaying to leptons were suppressed by requiring no identified electron or muon with energy larger than 10% or 7.5% of \sqrt{s} , respectively. Particles were identified as muons if there was at least one muon chamber hit associated to a track or if the size and longitudinal profile of the energy deposits associated to a track in the hadronic calorimeters were consistent with a minimum ionizing particle. Electron identification was based on the reconstructed showers in the electromagnetic calorimeters associated to charged particle tracks.

The expected composition of the residual sample after the preselection stage is shown in Table 1, together with the number of selected events at each centre-of-mass energy. At this level of the selection, the fraction of signal events is between 6% and 10% at all the energy points.

The final selection of $e^- \bar{\nu}_e q \bar{q}'$ events was based on a Neural Network analysis. The input variables were chosen to provide a good separation from the main residual backgrounds after preselection. The first set of variables, listed below, discriminated the signal from $q \bar{q}(\gamma)$ events:

⁵The definition of neutral current (NC) and charged current (CC) four-fermion processes of Ref. [19] are used throughout the text.

⁶Acoplanarity is defined as the supplement of the angle between the projections of the two hadronic jets in the plane transverse to the beam direction.

\sqrt{s} (GeV)	$e^- \bar{\nu}_e q \bar{q}'$ signal	Other CC	NC	$q \bar{q}(\gamma)$	Total MC	Data
183 GeV	9.5	66.8	5.0	74.2	157.0 ± 0.7	167
189 GeV	32.5	195.6	25.7	204.5	462.8 ± 2.0	467
192-202 GeV	54.2	276.9	51.4	227.3	615.4 ± 1.7	675
205-207 GeV	55.6	240.5	54.4	194.9	549.2 ± 1.7	569

Table 1: Number of events expected from the contribution of different channels and observed in the data after preselection of $e^- \bar{\nu}_e q \bar{q}'$ events for the different years of data taking. “Other CC” indicates charged current processes different from the signal, “NC” indicates neutral current processes. Other final states, mainly $\gamma\gamma$, contribute less than 1% of the total number of events. The quoted errors on the total number of expected events (“Total MC”) are the ones due to limited Monte Carlo statistics.

- effective centre-of-mass energy after ISR, $\sqrt{s'}$, normalised to the centre-of-mass energy, \sqrt{s} [21];
- normalised sum of the particle momenta projected on to the thrust axis, P_l^{tot}/\sqrt{s} ;
- cosine of the polar angle of the missing momentum, $|\cos \theta_{miss}|$;
- normalised total missing momentum, P_{miss}^{tot}/\sqrt{s} ;
- normalised total transverse momentum with respect to the beam axis, P_t^{tot}/\sqrt{s} ;
- event thrust;
- $|90^\circ - \theta_{thrust}|$, where θ_{thrust} is the polar angle of the thrust axis.

A second set of variables suppressed $\tau \nu_\tau q \bar{q}'$ events, where the τ lepton produces an isolated particle or a low multiplicity jet, and $\nu \bar{\nu} q \bar{q}$ events, where the kinematic properties of the visible system should be consistent with the decay of a Z :

- maximum transverse momentum of any particle with respect to the nearest jet, P_{tJ}^{max} , when the particles are clustered using the LUCCLUS [22] algorithm with the parameter $d_{min} = 6.5$ GeV/ c ;
- invariant mass of the detected particles in the event rescaled by the ratio of the total centre-of-mass energy to the visible energy, $M_{vis} \cdot \sqrt{s}/E_{vis}$;
- Lorentz boost factor of the visible part of the event in the laboratory frame, $\beta = P^{tot}/E_{vis}$.

Distributions of some of these variables, at $\sqrt{s} = 200$ GeV, are shown in Figure 2. The Neural Network was trained on samples of simulated events including the signal, for which the output value was set to 1, and the main backgrounds, $q \bar{q}(\gamma)$ and four-fermion processes, with output set to 0. The distribution of the Neural Network output variable is shown in Figure 3. The whole data sample is included in the plot. The cut on the output variable was set at 0.5, the value for which the product of efficiency and purity was found to be maximum. In the region $50 \text{ GeV}/c^2 < M_{vis} \cdot \sqrt{s}/E_{vis} < 60 \text{ GeV}/c^2$ an excess of real data was found at each energy point in the final selected sample ($7.4 \pm 1.3\%$ of the total number of events in the real data compared to $4.2 \pm 0.2\%$ in the simulation). To account for this excess, a correction of 34 fb was added to the background cross-section at each energy point.

The efficiency of the selection for the signal, the expected background, the luminosity and the number of selected events in the data at the various centre-of-mass energies

\sqrt{s} (GeV)	ε (%)	σ_{bkg} (pb)	\mathcal{L}_{int} (pb ⁻¹)	N_{data}	$\sigma_{e\nu qq'}$ (pb)
183	36.3±1.4	0.504±0.010	51.6	28	0.107 ^{+0.300} _{-0.107}
189	37.0±1.5	0.506±0.011	153.8	110	0.565 ^{+0.190} _{-0.179}
192	36.7±1.0	0.502±0.011	24.5	15	0.300 ^{+0.469} _{-0.300}
196	35.2±0.6	0.504±0.009	72.0	49	0.502 ^{+0.290} _{-0.263}
200	36.1±0.6	0.502±0.007	81.8	58	0.574 ^{+0.269} _{-0.247}
202	37.5±1.0	0.503±0.010	39.7	30	0.674 ^{+0.391} _{-0.346}
205	38.3±1.6	0.556±0.009	66.2	62	0.994 ^{+0.324} _{-0.298}
207	39.2±1.5	0.560±0.010	129.7	114	0.814 ^{+0.217} _{-0.204}

Table 2: Performance (signal efficiency, ε , background cross-section, σ_{bkg} , integrated luminosity, \mathcal{L}_{int} , and number of selected events, N_{data}) of the $e^-\bar{\nu}_e q\bar{q}'$ event selection and measured cross-sections at the centre-of-mass energies considered in the analysis. The errors quoted on efficiencies and backgrounds are the ones due to limited Monte Carlo statistics.

are reported in Table 2, together with the cross-section for the hadronic channel alone, evaluated from a fit of Poisson probabilities to the observed numbers of events.

Efficiencies and backgrounds at $\sqrt{s} = 207$ GeV were found to be compatible in the two periods with the sector S6 of the TPC on or off, and results have been merged in the table. The purity of the final selected sample is between 25% and 30%. The main contamination is due to $WW \rightarrow \tau\nu_\tau q\bar{q}'$ events.

3.2 Selection of leptonic events

The experimental signature of the leptonic channel, $e^+e^- \rightarrow e^-\bar{\nu}_e l^+\nu_l$, is the presence of a high energy lepton accompanied by a large missing momentum and no other significant energy deposition in the detector. The analysis was optimised for final state leptons that are electrons or muons. In both channels, the contribution from $e\nu_e\tau\nu_\tau$ events was considered as part of the background.

The main backgrounds for the leptonic channel are the radiative production of two leptons, $e^+e^- \rightarrow l^+l^-(\gamma)$, $e^+e^- \rightarrow W^+W^-$ events and two-photon collisions.

Events were selected if exactly one well measured charged particle was reconstructed. The quality of the track measurement was assessed as follows:

- relative error on the momentum, $\Delta p/p$, smaller than 100%;
- track length greater than 20 cm;
- polar angle θ between 10° and 170°;
- impact parameter in the transverse plane, $|IP_{R\phi}|$, smaller than 4 cm, and that along the beam direction, $|IP_z|$, smaller than 3 cm / $\sin\theta$.

Loose identification criteria were applied, requiring associated hits in the muon chambers or a significant energy deposit in the electromagnetic calorimeter. For electrons, the acceptance was restricted to the barrel region, $|\cos\theta| < 0.72$, and the best determination of the electron energy was estimated by combining the momentum measurement from the tracking devices and the measurement of the energy deposited in the calorimeters. Any

\sqrt{s} (GeV)	ε (%)	σ_{bkg} (fb)	\mathcal{L}_{int} (fb $^{-1}$)	N_{data}	$\sigma_{e\nu\mu\nu}$ (fb)
183	44.8 \pm 2.8	18.8 \pm 1.6	0.0516	7	< 526 at 95% C.L.
189	47.2 \pm 1.7	19.1 \pm 1.2	0.1538	5	< 106 at 95% C.L.
192	48.4 \pm 2.7	18.6 \pm 1.6	0.0245	1	< 369 at 95% C.L.
196	49.0 \pm 1.6	20.2 \pm 1.3	0.0720	4	< 218 at 95% C.L.
200	45.2 \pm 2.5	22.8 \pm 1.4	0.0818	7	< 304 at 95% C.L.
202	45.3 \pm 1.7	24.0 \pm 2.0	0.0397	5	< 531 at 95% C.L.
205	45.4 \pm 1.7	20.3 \pm 1.7	0.0662	2	< 172 at 95% C.L.
207	46.3 \pm 1.8	23.0 \pm 1.6	0.1297	8	< 191 at 95% C.L.

Table 3: Performance (signal efficiency, ε , background cross-section, σ_{bkg} , integrated luminosity, \mathcal{L}_{int} , and number of selected events, N_{data}) of the $e^-\bar{\nu}_e\mu^+\nu_\mu$ event selection at the centre-of-mass energies considered in the analysis. The errors quoted on efficiencies and backgrounds are the ones due to limited Monte Carlo statistics.

other energy deposit in the detector unassociated to the lepton candidate was required not to exceed 2 GeV. In addition, the presence of tracks not fulfilling the quality criteria listed above was used to veto the event. The acceptance was restricted to the kinematic region of W decays by requiring the lepton momentum to lie below 45% of \sqrt{s} and its transverse momentum to exceed 12% of \sqrt{s} .

A large residual contamination was still present, due to cosmic-ray events in the muon channel and to Compton scattering of a radiated photon in the electron channel. The former were suppressed by tightening the selections on the track impact parameters to $|IP_{R\phi}| < 0.2$ cm and $|IP_z| < 2$ cm for the muons. Compton scattering can mimic the $W^+ \rightarrow e^+\nu_e$ signal when the photon balancing the electron in the transverse plane is lost in the dead region between the barrel and forward electromagnetic calorimeters. Therefore events were rejected if a signal was found in the hermeticity counters at an azimuthal angle larger than 90° from the electron.

The distributions in data and simulation of the momentum of selected single muons and of the energy of selected single electrons are shown in Figure 4.

The performance of the analysis at the various centre-of-mass energy values and the results obtained are reported in Tables 3 and 4, respectively, for the $e^-\bar{\nu}_e\mu^+\nu_\mu$ and $e^-\bar{\nu}_ee^+\nu_e$ channels. Due to the low statistics of selected events only the upper limits of cross-sections at 95% C.L. are given for each individual energy point. The limits were derived following a Bayesian approach from the integration of the Poissonian probabilities constructed with the number of events selected in the data and predicted in the simulation. For the electron channel a difference was found for efficiencies and backgrounds corresponding to the two periods at $\sqrt{s} = 207$ GeV with TPC sector S6 on or off, and in Table 4 the weighted averages of the two are shown. Compatible values were found for the muon channel.

3.3 Study of systematic uncertainties

The main source of systematic uncertainty in the present measurement is the knowledge of the background level in the selected samples. In particular, as can be seen from

\sqrt{s} (GeV)	ε (%)	σ_{bkg} (fb)	\mathcal{L}_{int} (fb $^{-1}$)	N_{data}	$\sigma_{e\nu e\nu}$ (fb)
183	37.2 \pm 3.3	36.4 \pm 2.5	0.0516	3	< 316 at 95% C.L.
189	35.6 \pm 2.1	38.6 \pm 2.5	0.1538	13	< 268 at 95% C.L.
192	35.6 \pm 2.1	43.1 \pm 2.5	0.0245	1	< 468 at 95% C.L.
196	35.5 \pm 2.1	44.4 \pm 2.5	0.0720	4	< 248 at 95% C.L.
200	32.3 \pm 1.9	41.1 \pm 2.5	0.0818	6	< 324 at 95% C.L.
202	31.0 \pm 2.0	40.9 \pm 2.5	0.0397	3	< 508 at 95% C.L.
205	29.6 \pm 3.0	38.3 \pm 2.6	0.0662	3	< 287 at 95% C.L.
207	29.0 \pm 2.1	38.4 \pm 2.9	0.1297	11	< 352 at 95% C.L.

Table 4: Performance (signal efficiency, ε , background cross-section, σ_{bkg} , integrated luminosity, \mathcal{L}_{int} , and number of selected events, N_{data}) of the $e^-\bar{\nu}_e e^+\nu_e$ event selection at the centre-of-mass energies considered in the analysis. The errors quoted on efficiencies and backgrounds are the ones due to limited Monte Carlo statistics.

Table 1, in the hadronic channel selection there is an excess of data of $(5\pm 2)\%$ with respect to the expectation at the preselection stage, at which the sample consists mainly of background events. Rescaling the background at the final stage of the selection by this factor leads to an average decrease of 69 ± 28 fb of the measured cross-section. This was considered as a systematic error fully correlated between the energy points. The correction factor added to the background cross-section, accounting for the excess of real data in the region $50 \text{ GeV}/c^2 < M_{vis} \cdot \sqrt{s}/E_{vis} < 60 \text{ GeV}/c^2$, was known with a statistical uncertainty of ± 10 fb. This leads to a systematic error on $\sigma_{e\nu qq'}$ of ± 26 fb, fully correlated between the energy points.

Possible inaccuracies in the modelling of background processes were evaluated by comparing different Monte Carlo generators. The only effect was found in the $q\bar{q}(\gamma)$ channel: using the ARIADNE [23] event generator instead of PYTHIA, the background estimate was 508 ± 14 fb instead of 502 ± 7 fb in the final $e^-\bar{\nu}_e q\bar{q}'$ sample selected at 200 GeV. The largest of the statistical errors of the ARIADNE and PYTHIA samples was taken as a systematic error. The total systematic error on the background cross-section, due to the modelling of $q\bar{q}(\gamma)$ process and to the limited simulation statistics (see Table 2), amounts approximately to $\pm 3\%$ in the hadronic channel.

In the leptonic channels the systematic error on the background cross-section due to the limited simulation statistics (see Tables 3 and 4) amounts approximately to $\pm 6\%$.

From a comparison of dimuon events in data and simulation, the tracking efficiency, ε_{track} , of DELPHI was found to be 0.5% higher in the simulation. This value was assumed as a systematic error. This has a negligible effect on the background, while it affects the selection efficiency of the signal for leptonic decays of the W .

The uncertainty on the efficiency of the electron identification, ε_e , was estimated by comparing a sample of Bhabha events in data and simulation. The discrepancy was at the level of 2%. The trigger efficiency for the leptonic events is known with an error better than 1%. This leads to a systematic error negligible compared to the other sources considered.

The luminosity is known with a total relative error of $\pm 0.6\%$.

Systematic effect	Error on $\sigma_{e\nu q\bar{q}'}$ (pb)	Error on $\sigma_{e\nu\mu\nu}$ (pb)	Error on $\sigma_{e\nu e\nu}$ (pb)
$\Delta\sigma_{bkg}(e\nu_e q\bar{q}')$ from preselection	0.069	-	-
$\Delta\sigma_{bkg}(e\nu_e q\bar{q}')$ from $M_{vis} \cdot \sqrt{s}/E_{vis}$	0.026	-	-
$\Delta\sigma_{bkg}(e\nu_e q\bar{q}') \pm 3\%$	0.042	-	-
$\Delta\sigma_{bkg}(e\nu_e \mu\nu_\mu) \pm 6\%$	-	0.003	-
$\Delta\sigma_{bkg}(e\nu_e e\nu_e) \pm 6\%$	-	-	0.008
$\Delta\varepsilon(e\nu_e q\bar{q}')$ due to simulation statistics	0.010	-	-
$\Delta\varepsilon(e\nu_e l\nu_l)$ due to simulation statistics	-	0.007	0.006
$\Delta\varepsilon(e\nu_e l\nu_l)$ due to ε_{track}	-	0.002	0.002
$\Delta\varepsilon(e\nu_e e\nu_e)$ due to ε_e	-	-	0.006
Luminosity $\pm 0.6\%$	0.012	0.001	0.001
Total	0.086	0.008	0.012

Table 5: Contributions to the systematic uncertainty on the $e^-\bar{\nu}_e q\bar{q}'$, $e^-\bar{\nu}_e \mu^+ \nu_\mu$ and $e^-\bar{\nu}_e e^+ \nu_e$ cross-sections at $\sqrt{s} = 200$ GeV. The selection efficiency, ε , is as defined in tables 2, 3 and 4; ε_{track} is the overall tracking efficiency in DELPHI, and ε_e is the electron identification efficiency.

3.4 Total single- W cross-section

The total single- W cross-section is defined as:

$$\sigma_{evff'} = \sigma_{e\nu q\bar{q}'} + 2 \times \sigma_{e\nu\mu\nu} + \sigma_{e\nu e\nu}, \quad (4)$$

where the factor two accounts for the $e^-\bar{\nu}_e \tau^+ \nu_\tau$ channel, not measured in the present analysis, assuming $\mu - \tau$ universality. This assumption introduces a theoretical error at the level of $\sim 3\%$ on the $e^-\bar{\nu}_e \tau^+ \nu_\tau$ estimation.

The effects of the uncertainties listed in the previous section on the measurement of the $e^-\bar{\nu}_e f f'$ cross-section at $\sqrt{s}=200$ GeV are given in Table 5. The total systematic error, obtained from the sum in quadrature of the individual contributions, is at the level of $\pm 9\%$. For the measurement at the other centre-of-mass energies, the same relative error was assumed.

The values of $\sigma_{evff'}$ measured at the different centre-of-mass energies together with their statistical and systematic errors are shown in Table 6.

4 Single- Z analysis

In the single γ^*/Z analysis, decays of the vector boson into hadronic and $\mu^+ \mu^-$ final states were considered. Both final states are characterized by an electron scattered at large angle with respect to the incoming direction. The other electron, lost in the beam pipe, results in a missing momentum pointing along the beam direction.

4.1 Selection of hadronic events

The experimental signature of these events consists of a pair of jets produced in the hadronic decay of the γ^*/Z recoiling against an electron. To maximize the sensitivity

\sqrt{s} (GeV)	$\sigma_{eff'} \text{ (pb)}$
183	$0.69^{+0.41}_{-0.23} \pm 0.06$
189	$0.75^{+0.22}_{-0.20} \pm 0.07$
192	$0.39^{+0.54}_{-0.31} \pm 0.04$
196	$0.68^{+0.33}_{-0.28} \pm 0.06$
200	$0.96^{+0.33}_{-0.29} \pm 0.09$
202	$1.24^{+0.51}_{-0.42} \pm 0.11$
205	$1.06^{+0.36}_{-0.30} \pm 0.10$
207	$1.14^{+0.26}_{-0.24} \pm 0.10$

Table 6: Total single-W cross-section, as defined in the text (eq. 4), as measured at the different centre-of-mass energies considered in the analysis. The first error is statistical and the second one is systematic.

of the analysis in the widest possible range of invariant masses of the γ^*/Z , the event selection was performed in three steps:

1. a loose preselection of events;
2. the identification of an isolated electron;
3. the final selection of signal events, optimized differently in two ranges of the invariant mass of the hadronic system, $m_{q\bar{q}}$, according to the most relevant background process in each region.

The preselection of events consisted of the following requirements:

- at least five charged particles in the event with at least one in the TPC with a measured transverse momentum larger than 2.5 GeV/ c , in order to select hadronic events;
- the presence of at least one electron candidate selected by requiring an energy deposit in the electromagnetic calorimeters $E_e > 3$ GeV, with an associated charged particle with $|\cos \theta_e| < 0.985$, corresponding to the acceptance of the DELPHI's forward and barrel electromagnetic calorimeters;
- in events with more than one reconstructed electromagnetic shower, the energy of the second most energetic shower was required to be less than $0.6E_{beam}$. This condition was imposed in order to reject events from Bhabha scattering.

The electron candidates were then retained if they satisfied the following criteria:

- in the barrel region ($42^\circ < \theta < 138^\circ$), the track parameters were required to be consistent with those of the shower measured by the electromagnetic calorimeter, with the additional requirement, for showers with energy higher than 30 GeV, that the energy deposited in the hadronic calorimeter did not exceed 10% of that deposited in the electromagnetic calorimeter;
- in the forward region ($10^\circ < \theta < 32^\circ$ and $148^\circ < \theta < 170^\circ$), the energy of the shower, reconstructed by re-clustering the energy deposits compatible with a single electromagnetic shower, was required to be compatible with the momentum of exactly one track measured in DELPHI's vertex detector and very forward tracker, and with the momentum of no more than one track measured in the inner detector and TPC (see [10,11]) for detailed description of these detectors);

	γ^*/Zee	WW	$Z(\gamma)$	$\gamma\gamma$	Others	Total MC	Data
183 GeV							
Preselection	24.2	202.9	560.5	160.3	149.9	1097.8	1238
e ident.	18.2	75.5	23.0	21.7	58.1	196.5	195
Signal selection	11.4 ± 0.2	0.4 ± 0.1	2.4 ± 0.3	0.8 ± 0.8	1.3 ± 0.1	16.3 ± 0.9	23
189 GeV							
Preselection	73.5	647.4	1487.6	434.1	426.6	3069.2	3470
e ident.	55.9	244.2	65.7	62.6	168.2	596.6	577
Signal selection	34.9 ± 0.4	1.4 ± 0.2	6.5 ± 0.7	3.3 ± 1.2	4.5 ± 0.5	50.7 ± 1.5	54
192-202 GeV							
Preselection	113.1	985.1	1946.4	669.4	608.1	4322.0	5016
e ident.	85.4	382.9	87.0	70.5	237.3	863.1	915
Signal selection	54.8 ± 0.5	2.7 ± 0.2	9.4 ± 0.6	2.6 ± 0.7	6.0 ± 0.3	75.6 ± 1.0	78
205-207 GeV							
Preselection	110.1	938.2	1620.6	654.2	562.2	3885.3	4034
e ident.	83.5	374.4	75.5	78.7	212.5	824.6	786
Signal selection	54.6 ± 0.5	2.9 ± 0.2	8.8 ± 0.5	1.9 ± 0.9	6.1 ± 0.2	74.3 ± 1.1	76

Table 7: Number of events expected from the contributions of different channels and observed in the data at different stages of the γ^*/Zee selection (hadronic channel) for the different years of data taking. The column labelled “ $\gamma\gamma$ ” refers to resolved two-photon events. The column labelled “Others” includes other four-fermion processes, namely $eeqq$ outside the signal definition and γ^*/Zee with fully leptonic final state, and events from Bhabha scattering, the four-fermion processes supplying the more important contribution.

- the angle, α_1 , of candidate tracks with respect to the closest charged particle with momentum $p > 0.5$ GeV/ c had to lie in the range $15^\circ < \alpha_1 < 170^\circ$, where the upper limit was imposed to reject events from Bhabha scattering left in the sample at this stage of the selection;
- the angle, α_2 , of candidate tracks with respect to the second closest charged particle with momentum $p > 0.5$ GeV/ c was required to satisfy the condition $\alpha_2 > 40^\circ$.

Electrons from conversions or from decays were further suppressed by requiring their impact parameters with respect to the primary interaction vertex to be within the range $|IP_{R\phi}| < 0.35$ cm in the transverse plane and $|IP_z| < 1$ cm along the beam line.

The charged and neutral particles were then clustered into two jets with the Durham algorithm [24], excluding the tag electron. Events for which the jet resolution variable that separates the three-jet topology from the two-jet topology, $y_{3 \rightarrow 2}$, was smaller than 10^{-4} were rejected. For the final selection a constrained kinematic fit of the event, imposing energy and momentum conservation, was then performed assuming a topology of signal events with two jets, a visible electron and one lost along the beam line. The four-momentum of the invisible electron was chosen to be $(0, 0, Q_e E, E)$ with Q_e the charge of the tagged electron. Fits with a χ^2 probability smaller than 10^{-5} were rejected. The final selection of signal events was then performed using the fitted kinematic variables for the tagged electron and the hadronic system. It was required that the following conditions be satisfied:

mass range (GeV/ c^2)	γ^*/Zee	WW	$Z(\gamma)$	$\gamma\gamma$	Others	Total MC	Data
$15 < m_{q\bar{q}} < 60$	49.2 ± 0.5	0.2 ± 0.1	3.6 ± 0.4	4.2 ± 1.2	9.4 ± 0.4	66.7 ± 1.5	80
$m_{q\bar{q}} > 60$	106.5 ± 0.5	7.2 ± 0.4	23.5 ± 1.0	4.3 ± 1.3	8.5 ± 0.2	150.1 ± 1.8	151

Table 8: Number of events expected from the contributions of different channels and observed in the data at the end of the γ^*/Zee selection (hadronic channel) for the overall LEP2 sample, in the two invariant mass ranges. The column labelled “ $\gamma\gamma$ ” refers to resolved two-photon events. The column labelled “Others” includes other four-fermion processes, namely $eeqq$ outside the signal definition and γ^*/Zee with fully leptonic final state, and events from Bhabha scattering, the four-fermion processes supplying the more important contribution.

- $Q_e \cos \theta_{miss} > 0.95$, with θ_{miss} being the polar angle of the missing momentum computed before the kinematic fit;
- $Q_e \cos \theta_e > -0.5$, with θ_e being the polar angle of the tagged electron.

The distributions of these variables after the electron identification cuts are shown in Figure 5 for the real and simulated data. For $m_{q\bar{q}} < 60$ GeV/ c^2 , where the dominant background consisted of resolved $\gamma\gamma$ collisions, events with $Q_e \cos \theta_e > 0.9$ and $E_e > 0.75 E_{beam}$ were also rejected. The numbers of selected data candidates and different background contributions after each selection step are shown in Table 7 for the different years of data-taking, while Table 8 shows the composition of the entire sample after the final selection in the two mass ranges. An excess of data of about 10% is observed at preselection level mostly due to imperfectly simulated events from Bhabha scattering. The efficiency of the selection on the signal, the expected background and the number of selected events in the data at the eight centre-of-mass energies are reported in Table 9, together with the evaluated cross-section.

The distribution of the invariant mass of the hadronic system after the kinematic fit is shown in Figure 6 for the overall LEP2 sample. The peak in the invariant mass distribution around the Z mass corresponds to events for which the contribution of the Zee process is dominant.

4.2 Selection of leptonic events

The search was restricted to events with γ^*/Z going into a $\mu^+\mu^-$ pair with invariant mass above 60 GeV/ c^2 . The general features are the same as for the hadronic channel with jets replaced by muons. Thus a three-track signature, of two high-momentum muons and one e^+ or e^- , scattered at large angle, is expected in the detector. The signal selection criteria on angular distributions were similar to those used in the hadronic channel.

In the preselection the event was required to have exactly three tracks fulfilling the following criteria:

- fractional error on the momentum $\Delta p/p < 50\%$;
- impact parameter in the transverse plane $|IP_{R\phi}| < 0.5$ cm and along the beam direction $|IP_z| < 3$ cm;
- at least one associated hit in the Vertex Detector.

$$\gamma^*/Z \rightarrow q\bar{q} \quad (15 < m_{q\bar{q}} < 60 \text{ GeV}/c^2)$$

\sqrt{s} (GeV)	ε (%)	σ_{bkg} (pb)	\mathcal{L}_{int} (pb ⁻¹)	N_{data}	σ (pb)
183	30.3±0.8	0.015±0.002	52.0	11	0.65 ^{+0.23} _{-0.19} ± 0.03
189	30.7±0.8	0.030±0.006	153.5	16	0.24 ^{+0.09} _{-0.08} ± 0.02
192	32.1±0.8	0.027±0.006	25.1	6	0.66 ^{+0.35} _{-0.26} ± 0.04
196	29.9±0.8	0.021±0.004	75.9	14	0.55 ^{+0.18} _{-0.15} ± 0.03
200	29.4±0.8	0.026±0.005	82.8	6	0.16 ^{+0.12} _{-0.09} ± 0.02
202	29.0±0.8	0.026±0.005	40.3	2	0.08 ^{+0.15} _{-0.08} ± 0.03
205	29.8±0.7	0.021±0.004	75.9	12	0.46 ^{+0.17} _{-0.14} ± 0.03
207 TPC OK	28.3±0.9	0.019±0.004	84.1	4	0.25 ^{+0.10} _{-0.09} ± 0.02
TPC S6-off	27.4±0.7	0.030±0.014	51.4	9	

$$\gamma^*/Z \rightarrow q\bar{q} \quad (m_{q\bar{q}} > 60 \text{ GeV}/c^2)$$

\sqrt{s} (GeV)	ε (%)	σ_{bkg} (pb)	\mathcal{L}_{int} (pb ⁻¹)	N_{data}	σ (pb)
183	27.2±0.4	0.078±0.017	52.0	12	0.56 ^{+0.27} _{-0.22} ± 0.07
189	27.8±0.4	0.068±0.007	153.5	38	0.64 ^{+0.15} _{-0.14} ± 0.04
192	28.1±0.4	0.063±0.006	25.1	6	0.63 ^{+0.40} _{-0.30} ± 0.04
196	28.8±0.3	0.060±0.006	75.9	19	0.66 ^{+0.21} _{-0.18} ± 0.04
200	29.7±0.5	0.072±0.006	82.8	20	0.57 ^{+0.20} _{-0.17} ± 0.04
202	30.5±0.4	0.066±0.006	40.3	5	0.19 ^{+0.21} _{-0.16} ± 0.02
205	30.7±0.3	0.072±0.006	75.9	14	0.37 ^{+0.17} _{-0.15} ± 0.03
207 TPC OK	31.0±0.3	0.068±0.006	84.1	22	0.69 ^{+0.15} _{-0.14} ± 0.03
TPC S6-off	29.4±0.3	0.060±0.004	51.4	15	

$$\gamma^*/Z \rightarrow \mu^+\mu^- \quad (m_{\mu^+\mu^-} > 60 \text{ GeV}/c^2)$$

\sqrt{s} (GeV)	ε (%)	σ_{bkg} (fb)	\mathcal{L}_{int} (fb ⁻¹)	N_{data}	σ (fb)
183	27.4±1.1	0.6±0.2	0.0540	1	< 319 at 95% C.L.
189	26.2±1.0	1.1±0.4	0.1581	5	< 250 at 95% C.L.
192	26.3±1.0	0.7±0.2	0.0258	0	< 441 at 95% C.L.
196	26.7±1.0	1.3±0.3	0.0769	2	< 301 at 95% C.L.
200	27.2±1.0	1.2±0.3	0.0843	1	< 203 at 95% C.L.
202	26.7±1.0	0.9±0.2	0.0411	0	< 273 at 95% C.L.
205	26.4±1.0	0.6±0.2	0.0767	1	< 232 at 95% C.L.
207 TPC OK	26.1±1.0	1.1±0.3	0.0874	1	< 201 at 95% C.L.
TPC S6-off	27.5±1.0	0.8±0.2	0.0544	2	

Table 9: Performance (signal efficiency, ε , background cross-section, σ_{bkg} , integrated luminosity, \mathcal{L}_{int} , and number of selected events, N_{data}) of the γ^*/Zee event selection at the centre-of-mass energies considered in the analysis. The period with TPC sector 6 down is indicated as “207 TPC-S6 off”. Cross-sections for $\gamma^*/Z \rightarrow \mu^+\mu^-$ are expressed in femtobarns due to smaller values.

	γ^*/Zee	$(e^+e^-\mu^+\mu^-)_{bkg}$	Others	Total MC	Data
183 GeV					
Preselection	0.87 ± 0.03	6.3 ± 0.1	0.6 ± 0.1	7.8 ± 0.1	4
Final Selection	0.60 ± 0.02	0.008 ± 0.003	0.02 ± 0.01	0.63 ± 0.03	1
189 GeV					
Preselection	2.6 ± 0.1	19.2 ± 0.4	1.8 ± 0.2	23.6 ± 0.4	24
Final Selection	1.7 ± 0.1	0.03 ± 0.01	0.14 ± 0.06	1.91 ± 0.09	5
192-202 GeV					
Preselection	3.8 ± 0.1	26.3 ± 0.3	2.4 ± 0.1	32.5 ± 0.3	21
Final Selection	2.7 ± 0.1	0.04 ± 0.01	0.21 ± 0.03	2.93 ± 0.06	3
2000 205-207 GeV					
Preselection	3.7 ± 0.1	23.8 ± 0.3	2.3 ± 0.1	29.8 ± 0.3	39
Final Selection	2.6 ± 0.1	0.04 ± 0.01	0.15 ± 0.03	2.79 ± 0.06	4

Table 10: Number of events expected from the contributions of different channels and observed in the data at different stages of the γ^*/Zee selection (leptonic channel) for the different years of data taking. The column labelled “ $(e^+e^-\mu^+\mu^-)_{bkg}$ ” shows the numbers for the background events coming from all processes with $e^+e^-\mu^+\mu^-$ in the final state not fulfilling the signal definition criteria. All other background sources are collected inside the column labelled “Others”.

The sum of the charges of the three particles was required to be ± 1 . Possible photon conversions were removed according to the procedure described in [10] and requiring in addition the minimum opening angle of any track pair to be larger than 5° .

Since the event topology is simple, the particle identification required at least two tracks to be identified as leptons (μ or e) and at least one of them to be a muon. For muon identification loose criteria were applied, as in the case of single- W production (see Section 3.2). The flavour of the possible unidentified track was inferred from partial information taking into account the combination of the charges of the observed particles. In the case of $\mu^+x^-e^\pm$ or $x^+\mu^-e^\pm$, the unidentified track x was treated as μ . For $\mu^+\mu^-x^\pm$ the track x was taken as e^\pm . Since the efficiency of the identification of the electrons was smaller than for the muons, a majority of events with the $\mu^+\mu^-$ pair detected and an unidentified electron was accepted this way. This reduced dramatically the sensitivity of event selection, and hence the loss of efficiency, to the efficiency of electron identification (less than 5% drop of signal selection efficiency was observed after forcing the electron track to be always unidentified). Events with two tracks identified as electrons were rejected. At the preselection stage, the momentum of the e^\pm candidate had to be greater than $2 \text{ GeV}/c$, and the invariant mass of the $\mu^+\mu^-$ pair greater than $20 \text{ GeV}/c^2$.

Due to the stringent cut on low multiplicity of the event, the data reduction factor was large. For all energy points, 88 events were preselected and 94.0 ± 0.6 events were expected. At this stage most of the events came from other neutral current four-fermion processes with $e^+e^-\mu^+\mu^-$ in the final state but outside the kinematic limits of the signal definition (see Table 10). The remaining contributions came mainly from the neutral current four-fermion processes ($e^+e^- \rightarrow l_1^+l_1^-l_2^+l_2^-$ excluding the $e^+e^-\mu^+\mu^-$ case), from two-fermion processes ($e^+e^- \rightarrow \mu^+\mu^-(\gamma)$ and $e^+e^- \rightarrow \tau^+\tau^-(\gamma)$) and a small fraction from $e^+e^- \rightarrow W^+W^-$.

A kinematic fit was performed before applying the final selection cuts to the data. An electron lost along the beam line and no missing momentum in the transverse plane were assumed. The invariant mass of the $\mu^+\mu^-$ pair was recalculated if the probability of the kinematic fit was above 0.001. The high purity of this channel implies that events with lower fit probability still correspond to $e^+e^-\mu^+\mu^-$ production, but with a poorly measured visible electron; such events were therefore retained and the original uncorrected $\mu^+\mu^-$ invariant mass was kept. In agreement with the signal definition the $\mu^+\mu^-$ invariant mass was then required to be greater than $60 \text{ GeV}/c^2$, the momentum of the observed electron greater than $3 \text{ GeV}/c$ and its polar angle θ_e to satisfy the condition $Q_e \cos \theta_e > -0.5$, with Q_e being the charge of the observed electron.

Finally the allowed angular ranges for the direction of the Z/γ^* momentum and missing momentum were defined by the following conditions:

- $Q_e \cos \theta_{\mu^+\mu^-} < -0.8$, with $\theta_{\mu^+\mu^-}$ being the polar angle of the $\mu^+\mu^-$ system;
- $Q_e \cos \theta_{miss} > 0.8$, with θ_{miss} being the polar angle of the missing momentum computed before the kinematic fit.

After the final selection the background contribution is expected to be less than 10% of the total selected events. The remaining background from processes with $e^+e^-\mu^+\mu^-$ in the final state which was dominant at the preselection level was reduced to about 1%.

The efficiency of the selection of the signal, the expected background and the number of selected events in the data for all centre-of-mass energies are reported in Table 9. Due to the low statistics of selected events only the upper limits of cross-sections at 95% C.L. are given for each individual energy point. The limits were derived following a Bayesian approach from the integration of the Poissonian probabilities constructed with the number of events selected in the data and predicted in the simulation. In total 13 events were selected and 8.3 ± 0.1 events were expected from data in the energy range from 183 GeV to 207 GeV. The $\mu^+\mu^-$ invariant mass distribution is shown in Figure 6.

The distributions of the energy and of the signed angle, $Q_e \cos \theta_e$, of the tag electron after the kinematic fit for hadronic and $\mu^+\mu^-$ events with $m_{f\bar{f}} > 60 \text{ GeV}/c^2$, are shown in Figure 7 summed over all the centre-of-mass energies. The observed spectra are in agreement with the predictions from the simulation.

4.3 Systematic uncertainties

The measurement uncertainty is dominated by the limited real data statistics.

In the hadronic channel three sources of systematic errors were considered: the efficiency in the electron selection procedure, the modelling of the contribution from two-photon events, which represents the largest background component in the low invariant mass region, and the modelling of the fragmentation in the $q\bar{q}(\gamma)$ contribution, which represents the largest background component in the high invariant mass region.

The uncertainty on the efficiency of the electron identification was estimated by comparing the number of selected events in the data and in the simulation for a sample enriched in WW events (about 85% purity) with at least one of the two W 's decaying, directly or in cascade, into a final state containing an electron. The same criteria for electron identification and isolation were adopted as in the Zee analysis, but the signal selection criteria were changed to maximize the product efficiency times purity of the WW selection. Assuming the Standard Model prediction for the WW cross-section, including the $\mathcal{O}(\alpha)$ electroweak corrections via the so-called Leading Pole Approximation [3], and attributing the entire discrepancy between the observed and the expected number of

events to the different electron identification efficiency in the data and in the simulation, the relative difference in the efficiency was found to be $\Delta\varepsilon_e/\varepsilon_e = (-2.2 \pm 3.6)\%$ where the error accounts both for the data and the simulation statistics. The error on the difference was used for the computation of the systematic error.

The uncertainty in modelling of two-photon events could arise from the bad modelling either of the direct or of the resolved photon contribution. As described in [18], in the region of single tag the direct component was simulated using the WPHACT generator and the resolved component using PYTHIA 6.143. To match the direct and resolved components in the region $m_{q\bar{q}} < 40 \text{ GeV}/c^2$ the WPHACT generator was run with constituent quark masses. The direct component of single tag events with $m_{q\bar{q}} > 40 \text{ GeV}/c^2$ was instead simulated with the WPHACT generator using current algebra quark masses. To gauge the effect of the different quark masses for the single tag low mass direct component, a fully simulated sample with current algebra quark masses only was used to evaluate the effect both on signal efficiency and on the background cross-section. The change in the quark mass does not affect the γ^*/Zee signal at any stage of the selection, while the background at the end of the selection is increased by about 5 fb in each invariant mass region. Concerning the resolved photon component, at $\sqrt{s} = 200 \text{ GeV}$ the cross-section of this background amounts, at the generator level, to about 10 fb in the γ^*ee signal region and 17 fb in the Zee one. A different generator, TWOGAM [25], predicts background cross-sections of 5 fb and 9 fb, respectively, in these two regions. As the topologies of the resolved photon and γ^*/Zee events are similar, the same selection efficiency was assumed for this background and the signal. Therefore the difference between the PYTHIA and TWOGAM predictions at the generator level, which is stable in the range $\sqrt{s} = 183 - 207 \text{ GeV}$, was taken as systematic error on the measured cross-section.

The uncertainty in modelling the fragmentation and hadronization in $q\bar{q}(\gamma)$ events was evaluated using a simulation sample produced with the ARIADNE generator. The background cross-sections were found to be larger, but within the statistical error, leading to a decrease of the measured cross-sections of $3 \pm 5 \text{ fb}$ in the low invariant mass region and $7 \pm 13 \text{ fb}$ in the high invariant mass one. The largest of the statistical errors from the ARIADNE and PYTHIA samples, 3 fb in the γ^*ee signal region and 9 fb in the Zee one, were taken as systematic error.

These three systematic uncertainties, together with the error on the luminosity, were taken as fully correlated at the different centre-of-mass energies, while the errors on the background cross-section and on the signal efficiency due to the limited simulation statistics were considered uncorrelated among the different energies.

The contributions of the sources of systematic uncertainty in the hadronic channel at 189 GeV are summarized in Table 11. The total systematic uncertainty amounts to $\pm 10\%$ in the region $15 < m_{q\bar{q}} < 60 \text{ GeV}/c^2$ and to $\pm 6\%$ for $m_{q\bar{q}} > 60 \text{ GeV}/c^2$.

The contributions of the different sources of systematic errors in the leptonic channel are summarized in Table 12. The main source of systematic error is the limited simulation statistics, both for the signal and for the background. The effect of the uncertainty on the efficiency of the electron identification was measured to be negligible using relaxed identification criteria. The total systematic uncertainty amounts to about $\pm 5\%$ per energy point. Assuming no energy correlation of the systematic errors, the overall systematic uncertainty on the energy averaged cross-section was estimated to be $\pm 2.5\%$, an order of magnitude smaller than the statistical uncertainty.

Systematic effect	Error on σ (pb)	
	$15 < m_{q\bar{q}} < 60 \text{ GeV}/c^2$	$m_{q\bar{q}} > 60 \text{ GeV}/c^2$
$\Delta\varepsilon_e$	0.009	0.022
$\Delta\sigma_{bkg}(\gamma\gamma)$ direct	0.005	0.005
$\Delta\sigma_{bkg}(\gamma\gamma)$ resolved	0.005	0.008
$\Delta\sigma_{bkg}(q\bar{q}\gamma)$ fragmentation	0.003	0.009
$\Delta\varepsilon$ due to simulation statistics	0.007	0.008
$\Delta\sigma_{bkg}$ due to simulation statistics	0.020	0.026
Luminosity $\pm 0.6\%$	0.002	0.005
Total	0.024	0.038

Table 11: Contributions to the systematic uncertainty on the γ^*/Zee cross-sections in the hadronic channel, in the two ranges of invariant mass of the hadronic system, at $\sqrt{s} = 189 \text{ GeV}$. The selection efficiency, ε , is as defined in table 9 and ε_e is the electron identification efficiency.

Systematic effect	Error on σ (fb)
$\Delta\varepsilon$ due to simulation statistics	1.8
$\Delta\sigma_{bkg}$ due to simulation statistics	1.4
Luminosity $\pm 0.6\%$	0.7
Total	2.4

Table 12: Contributions to the systematic uncertainty at $\sqrt{s} = 189 \text{ GeV}$ on the predicted γ^*/Zee cross-section in the leptonic channel. The selection efficiency, ε , is as defined in table 9. The systematic errors were conservatively considered to be the same for all centre-of-mass energies. The systematic due to the uncertainty on the electron identification efficiency was measured to be negligible.

5 Combined single boson cross-sections

The measured values for single boson cross-sections are compared with the Standard Model predictions obtained with WPHACT [12] as a function of the centre-of-mass energy. This dependency is shown in Figure 8 for single- W and single- Z production. The theoretical uncertainty on the predictions amounts to 5%. The overall compatibility with the Standard Model was checked by considering the ratio R of the measured to the predicted cross-sections. At each energy point a Poissonian probability function was constructed based on the number of observed events, the number of expected background events and the signal extraction efficiency. A maximum likelihood fit to the data of the global probability function, being the product over all probability functions for individual energies convoluted with a multidimensional Gaussian describing the correlated and uncorrelated systematic errors, was performed. The results were:

$$R(e\nu_e qq') = 1.20 \pm 0.18 \text{ (stat.)} \pm 0.14 \text{ (syst.)},$$

$$R(e\nu_e \mu \nu_\mu) = 1.06^{+0.27}_{-0.25} \text{ (stat.)} \pm 0.03 \text{ (syst.)},$$

$$R(e\nu_e e \bar{\nu}_e) = 1.07^{+0.38}_{-0.35} \text{ (stat.)} \pm 0.09 \text{ (syst.)},$$

$$R(eeq\bar{q}) = 1.22^{+0.17}_{-0.16} \text{ (stat.)} \pm 0.06 \text{ (syst.)} \quad 15 < m_{q\bar{q}} < 60 \text{ GeV}/c^2,$$

$$R(eeq\bar{q}) = 1.00^{+0.12}_{-0.11} \text{ (stat.)} \pm 0.05 \text{ (syst.)} \quad m_{q\bar{q}} > 60 \text{ GeV}/c^2,$$

$$R(ee\mu\bar{\mu}) = 1.59^{+0.51}_{-0.43} \text{ (stat.)} \pm 0.03 \text{ (syst.)} \quad m_{\mu^+\mu^-} > 60 \text{ GeV}/c^2,$$

where the systematic error represents only the experimental contribution. The values found show a good agreement with the Standard Model predictions.

Acknowledgements

We are greatly indebted to our technical collaborators, to the members of the CERN-SL Division for the excellent performance of the LEP collider, and to the funding agencies for their support in building and operating the DELPHI detector.

We acknowledge in particular the support of

Austrian Federal Ministry of Education, Science and Culture, GZ 616.364/2-III/2a/98,
FNRS-FWO, Flanders Institute to encourage scientific and technological research in the
industry (IWT), Belgium,

FINEP, CNPq, CAPES, FUJB and FAPERJ, Brazil,

Czech Ministry of Industry and Trade, GA CR 202/99/1362,

Commission of the European Communities (DG XII),

Direction des Sciences de la Matière, CEA, France,

Bundesministerium für Bildung, Wissenschaft, Forschung und Technologie, Germany,

General Secretariat for Research and Technology, Greece,

National Science Foundation (NSF) and Foundation for Research on Matter (FOM),

The Netherlands,

Norwegian Research Council,

State Committee for Scientific Research, Poland, SPUB-M/CERN/PO3/DZ296/2000,

SPUB-M/CERN/PO3/DZ297/2000, 2P03B 104 19 and 2P03B 69 23(2002-2004)

FCT - Fundação para a Ciência e Tecnologia, Portugal,

Vedecka grantova agentura MS SR, Slovakia, Nr. 95/5195/134,

Ministry of Science and Technology of the Republic of Slovenia,

CICYT, Spain, AEN99-0950 and AEN99-0761,

The Swedish Research Council,

Particle Physics and Astronomy Research Council, UK,

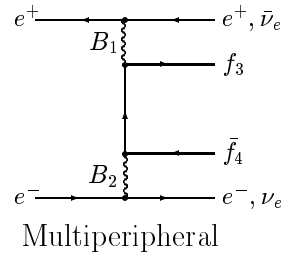
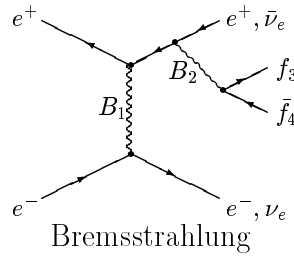
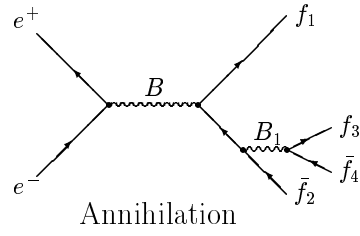
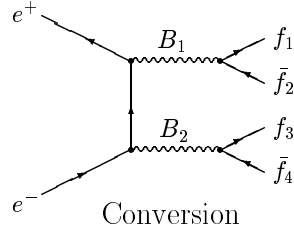
Department of Energy, USA, DE-FG02-01ER41155,

EEC RTN contract HPRN-CT-00292-2002.

References

- [1] F. Boudjema et al., *Standard Model Processes*, in *Physics at LEP2*, Vol.1, G. Altarelli, T. Sjöstrand and F. Zwirner (eds.), CERN 96-01 (1996) 207.
- [2] E. Gabrielli, *Single Weak Boson Production at CLIC*, in *Proc. Workshop on Physics at future accelerators*, Vol.2, J.H. Mulvey (ed.), CERN 87-07 (1987) 1;
K. Hagiwara et al., Nucl. Phys. **B365** (1991) 544.
- [3] M. Grünewald et al., *Four-fermion production in electron-positron collisions*, in *Reports of the working groups on precision calculations for LEP2 Physics*, S. Jadach, G. Passarino and R. Pittau (eds.) CERN 2000-009 (2000) 1.
- [4] S. Godfrey, P. Kalyniak and N. Romanenko, Phys. Rev. **D65** (2002) 033009.
- [5] DELPHI Collaboration, P. Abreu et al., Phys. Lett. **B502** (2001) 9.
- [6] DELPHI Collaboration, P. Abreu et al., Phys. Lett. **B515** (2001) 238.
- [7] ALEPH Collaboration, R. Barate et al., Phys. Lett. **B462** (1999) 389;
ALEPH Collaboration, S. Schael et al., Phys. Lett. **B605** (2005) 49.
- [8] L3 Collaboration, M. Acciarri et al., Phys. Lett. **B436** (1998) 417;
L3 Collaboration, M. Acciarri et al., Phys. Lett. **B487** (2000) 229;
L3 Collaboration, P. Achard et al., Phys. Lett. **B547** (2002) 151;
L3 Collaboration, P. Achard et al., Phys. Lett. **B561** (2003) 73.
- [9] OPAL Collaboration, G. Abbiendi et al., Phys. Lett. **B438** (1998) 391;
OPAL Collaboration, G. Abbiendi et al., Eur. Phys J. **C24** (2002) 1.
- [10] DELPHI Collaboration, P. Aarnio et al., Nucl. Instr. and Meth. **A303** (1991) 233;
DELPHI Collaboration, P. Abreu et al., Nucl. Instr. and Meth. **A378** (1996) 57.
- [11] V. Chabaud et al., Nucl. Instr. and Meth. **A368** (1996) 314;
P. Chochula et al., Nucl. Instr. and Meth. **A412** (1998) 304.
- [12] E. Accomando and A. Ballestrero, Comp. Phys. Comm. **99** (1997) 270;
E. Accomando, A. Ballestrero and E. Maina, Comp. Phys. Comm. **150** (2003) 166.
- [13] S. Jadach, B.F.L. Ward and Z. Wąs, Phys. Lett. **B449** (1999) 97;
S. Jadach, B.F.L. Ward and Z. Wąs, Comp. Phys. Comm. **130** (2000) 260.
- [14] D. Karlen, Nucl. Phys. **B289** (1987) 23.
- [15] S. Jadach, W. Placzek and B.F.L. Ward, Phys. Lett. **B390** (1997) 298.
- [16] T. Sjöstrand, Comp. Phys. Comm. **82** (1994) 74;
T. Sjöstrand et al., Comp. Phys. Comm. **135** (2001) 238.
- [17] F.A. Berends, P.H. Daverveldt and R. Kleiss, Comp. Phys. Comm. **40** (1986) 271, 285, 309.
- [18] A. Ballestrero et al., Comp. Phys. Comm. **152** (2003) 175.
- [19] D. Bardin et al., *Event Generators for WW Physics*, in *Physics at LEP2*, Vol.2, G. Altarelli, T. Sjöstrand and F. Zwirner (eds.), CERN 96-01 (1996) 3.
- [20] C. Peterson, T. Rönkvallsson and L. Lönnblad, Comp. Phys. Comm. **81** (1994) 185.
- [21] P. Abreu et al., Nucl. Instr. and Meth. **A427** (1999) 487.
- [22] T. Sjöstrand, Comp. Phys. Comm. **28** (1983) 229.
- [23] L. Lönnblad, Comp. Phys. Comm. **71** (1992) 15.
- [24] S. Catani et al., Phys. Lett. **B269** (1991) 432.
- [25] Š. Todorova-Nová et al., *Event generators for $\gamma\gamma$ physics*, in *Reports of the working groups on precision calculations for LEP2 Physics*, S. Jadach, G. Passarino and R. Pittau (eds.) CERN 2000-009 (2000) 219.

Abelian Classes



Nonabelian Classes

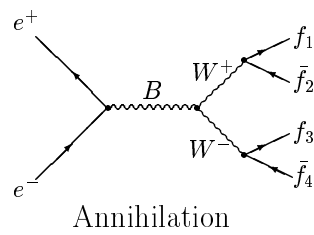
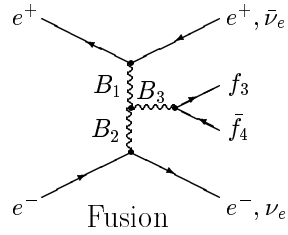


Figure 1: Four-fermion production classes of diagrams in e^+e^- annihilation following the convention of [1]: $B = Z, \gamma$ and $B_1, B_2, B_3 = Z, \gamma, W^\pm$. Diagrams involving Higgs boson exchange are not shown.

DELPHI

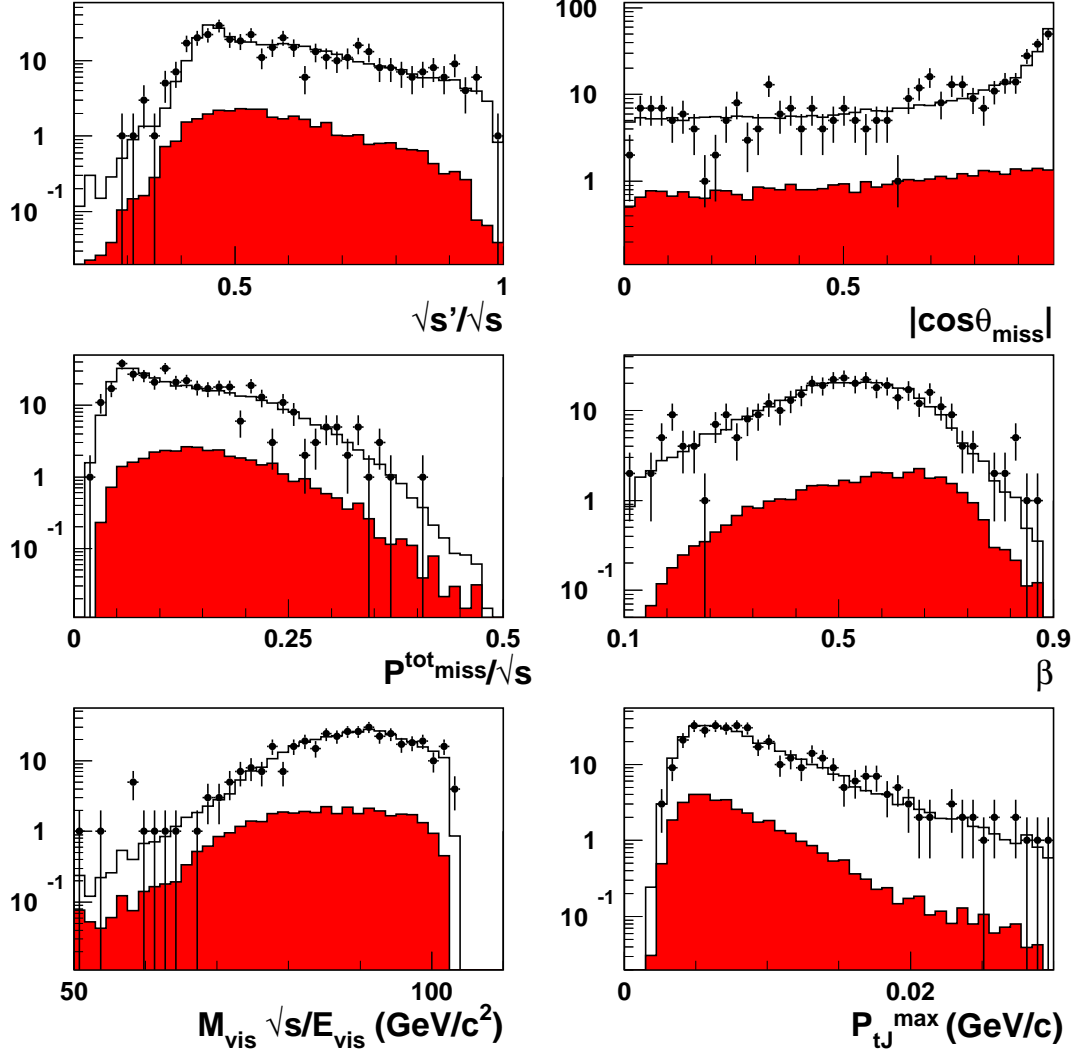


Figure 2: $e\nu_e W$ channel ($W \rightarrow q\bar{q}'$) at $\sqrt{s} = 200$ GeV. Distribution of some Neural Network input variables, as defined in the text, in the real data (points with error bars) and in the simulation of the Standard Model predictions (histograms) after the preselection stage (see text). The distributions of these variables for the $e\nu_e W$ signal are shown as well (filled histograms). The $|\cos \theta_{\text{miss}}|$ distribution (top-right) stops at 0.98, as explained in the text.

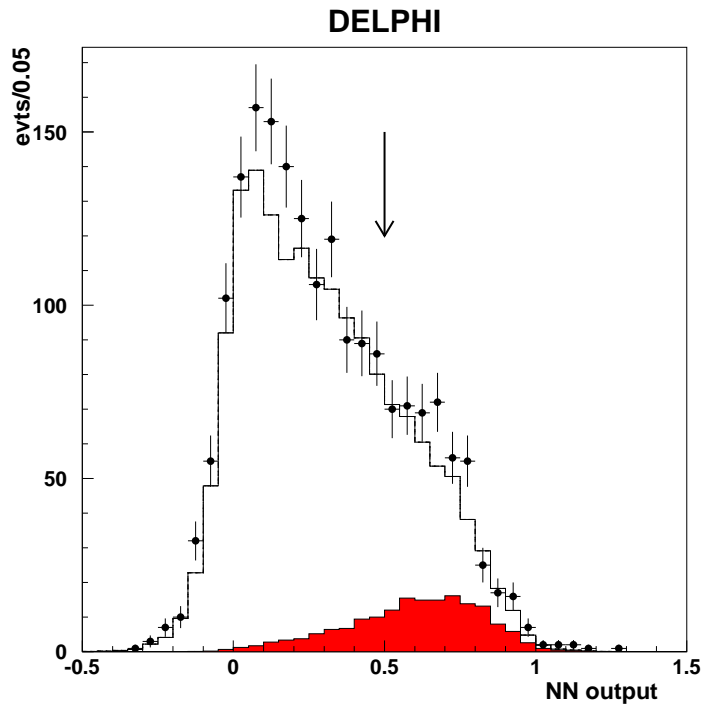


Figure 3: $e\nu_e W$ channel ($W \rightarrow q\bar{q}'$) summed over all centre-of-mass energies: distribution of the Neural Network output variable in the real data (points with error bars) and in the simulation of the Standard Model predictions (histograms). The filled histogram represents the single- W signal, the open area is the background expectation. The arrow indicates the cut applied on this variable for the final event selection.

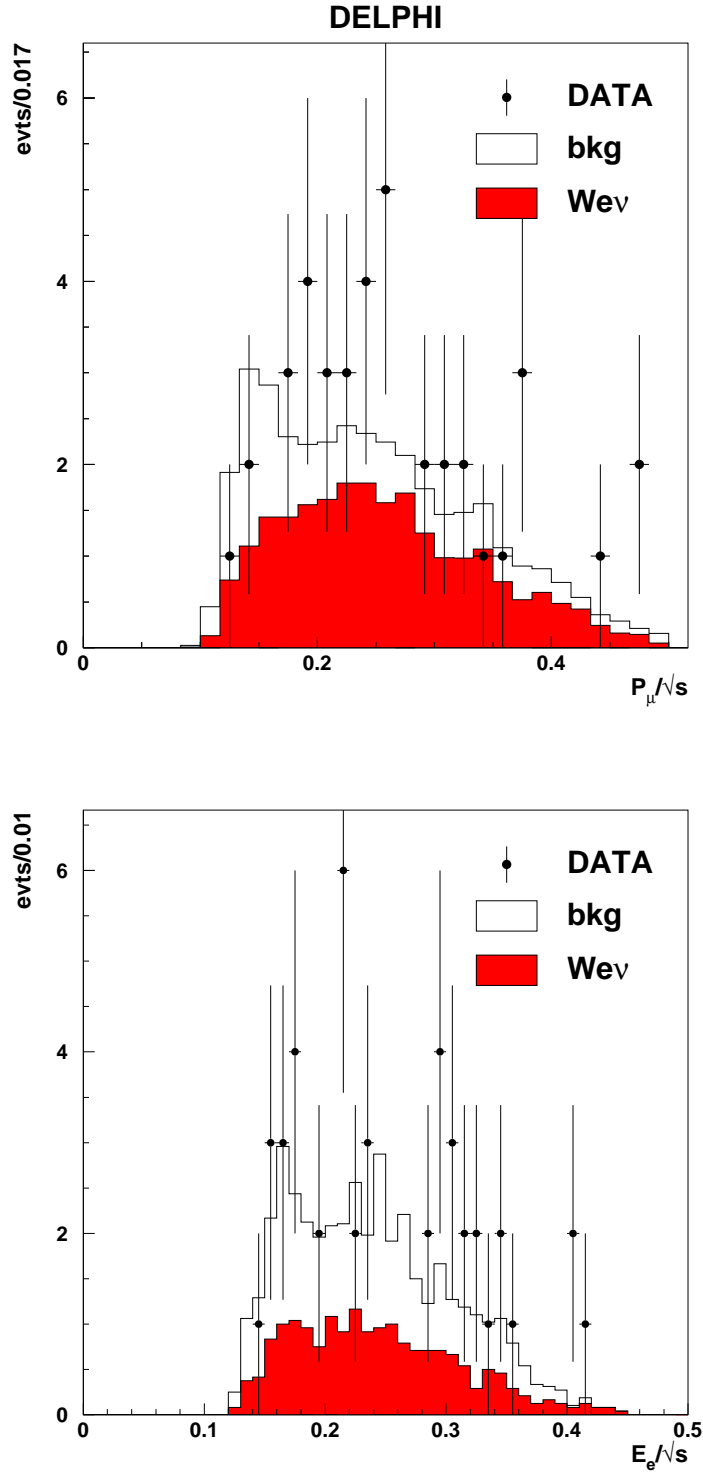


Figure 4: $e\nu_e W$ channel ($W \rightarrow l^+ \nu_l$) summed over all centre-of-mass energies: momentum distribution of the muon (*top*) and energy distribution of the electron (*bottom*) in the real data (points with error bars) and in the simulation of the Standard Model predictions (histograms) for the events selected at the end of the analysis. The filled histograms represent the single- W signal, the open area is the background expectation.

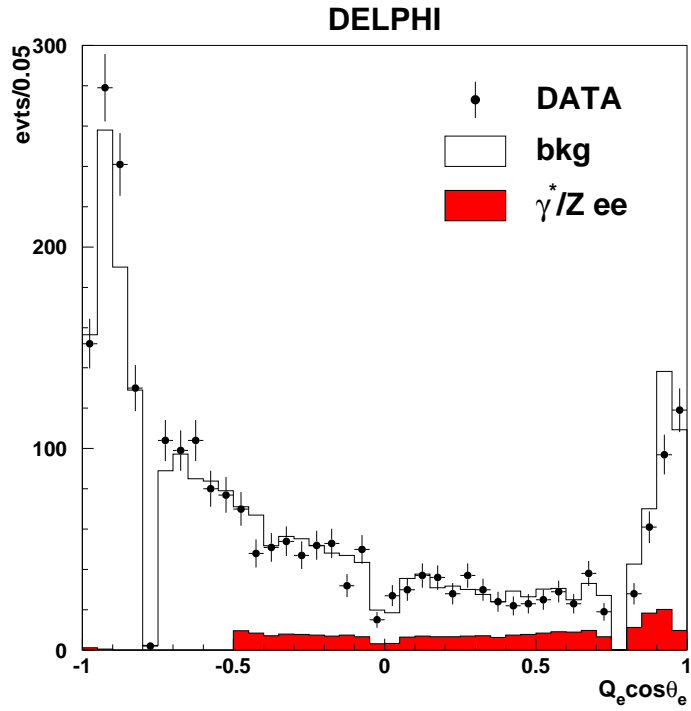
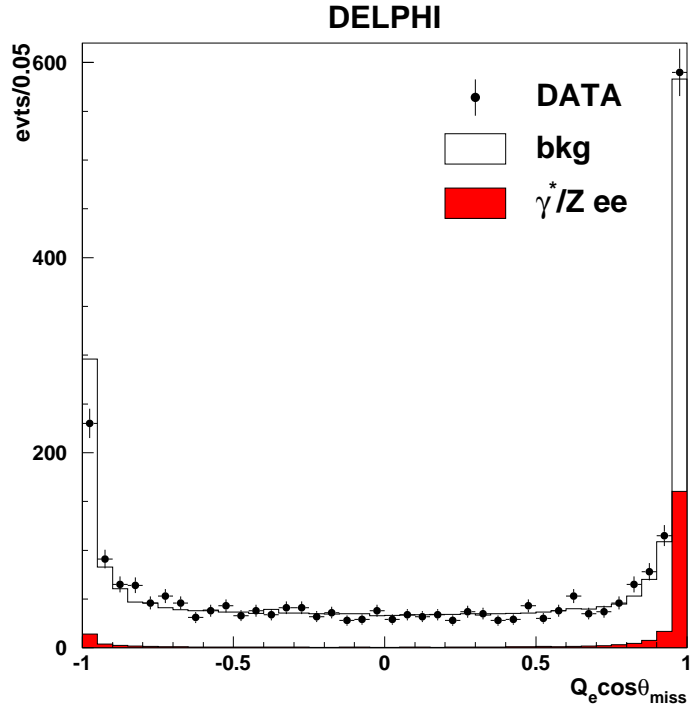


Figure 5: γ^*/Zee channel ($\gamma^*/Z \rightarrow q\bar{q}$) summed over all centre-of-mass energies: distributions of the variables used for the signal definition at the reconstruction level after the “electron identification” step (see Section 4.1), in the real data (points with error bars) and in the simulation of the Standard Model predictions (histograms). The γ^*/Zee signal is defined in the kinematic region described in Section 2.

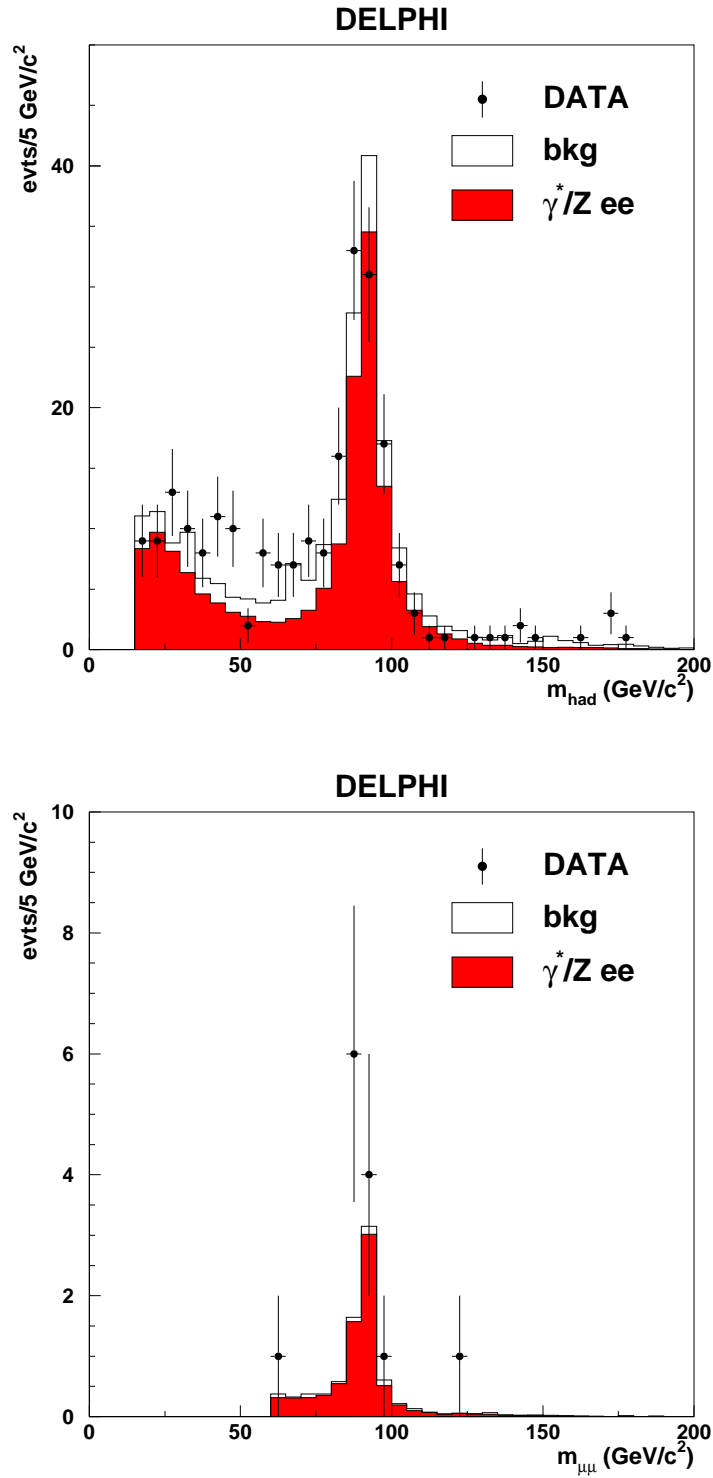


Figure 6: γ^*/Zee channel summed over all centre-of-mass energies: invariant mass distribution of the γ^*/Z system in the real data (points with error bars) and in the simulation of the Standard Model predictions (histograms) for hadronic (*top*) and $\mu^+\mu^-$ (*bottom*) final states, in the selected signal sample.

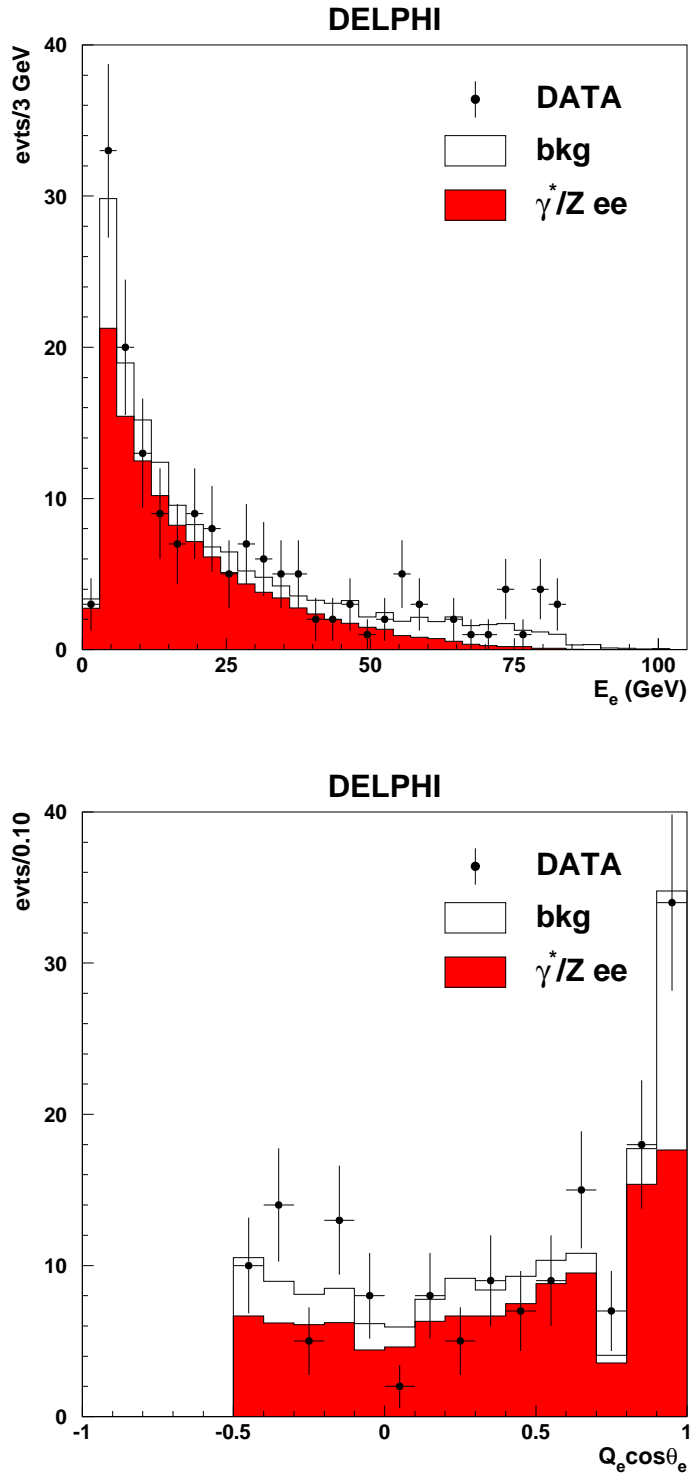


Figure 7: γ^*/Zee channel summed over all centre-of-mass energies: energy spectrum (*top*) and signed angle $Q_e \cos \theta_e$, (*bottom*) of the tag electron for hadronic and $\mu^+\mu^-$ final states with $m_{f\bar{f}} > 60 \text{ GeV}/c^2$, in the selected signal sample. The points with error bars represent real data, the histograms the simulation.

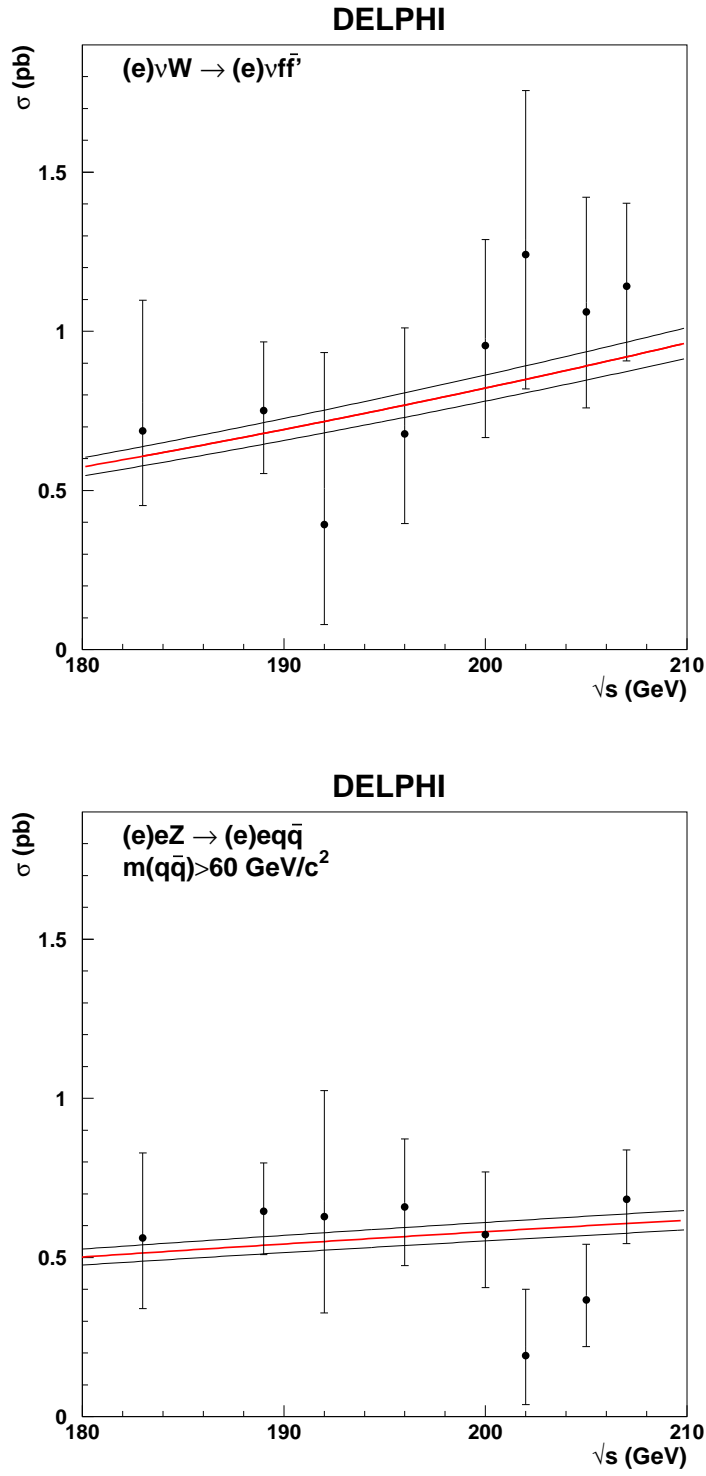


Figure 8: Cross-sections as a function of \sqrt{s} for the $e\nu_e W$ channel (*top*) and the Zee channel $Zee \rightarrow e^+e^-q\bar{q}$ (*bottom*). The solid curves are the Standard Model predictions, with a 5% uncertainty band, computed with WPHACT [12].